Remote Sensing of Environment 287 (2023) 113486

Contents lists available at ScienceDirect

Remote Sensing of Environment

journal homepage: www.elsevier.com/locate/rse

The many shades of red tides: Sentinel-2 optical types of highly-concentrated harmful algal blooms

Pierre Gernez [a,*], Maria Laura Zoffoli [b], Thomas Lacour [c], Tania Hernández Fariñas [d], Gabriel Navarro [e], Isabel Caballero [e], Tristan Harmel [f]

[a] Nantes Université, Institut des Substances et Organismes de la Mer, ISOMER, UR 2160, F-44000 Nantes, France
[b] Consiglio Nazionale delle Ricerche, Istituto di Scienze Marine (CNR-ISMAR), 00133, Rome, Italy
[c] Ifremer, PHYTOX, Laboratoire PHYSALG, F-44000 Nantes, France
[d] Ifremer, Laboratoire Environnement Ressources Normandie, Port en Bessin, France
[e] Consejo Superior de Investigaciones Científicas, Instituto de Ciencias Marinas de Andalucía, Puerto Real, Spain
[f] Magellium, 1 Rue Ariane, Ramonville-Saint-Agne, France

ARTICLE INFO

Edited by Menghua Wang

Keywords:
Phytoplankton
Ecology
Dinoflagellates
Cyanobacteria
Ciliate
mesodinium
noctiluca
lepidodinium
Pigments
REPHY
HAEDAT

ABSTRACT

Harmful algal blooms (HABs) have severe environmental and economic impacts worldwide. Improving HAB detection is crucial because massive blooms are likely to increase in both frequency and amplitude in the next decades due to global warming and escalating coastal eutrophication. While satellite remote sensing has proved useful to detect red tides and support HAB monitoring, the discrimination of the dominant bloom-forming species is still a challenge, all the more as the observation of highly concentrated phytoplankton patches can be hampered by a too coarse spatial resolution. Moreover, the majority of HAB studies generally had a regional focus, and a limited number of species were separately documented so far. Here, we provide a broader perspective for red tides remote sensing to better resolve HAB optical and taxonomical diversity. The main objective of the present study was to identify how many optical bloom types could be recognized with the high spatial resolution Sentinel-2 (S2) satellite mission. For that purpose, an extensive database of massive, nearly monospecific blooms, both documented in situ and using synchronous S2 observation was compiled. More than 100 S2 images of various red tides were selected worldwide. Altogether, the S2 database covered the typical reflectance spectra of 27 red tide forming species. The remote-sensing reflectance of each red tide was analysed to evaluate S2 ability to distinguish the dominant species of the bloom. A hierarchical clustering analysis suggested that six optical bloom types could be identified: (1) surface accumulation of cyanobacteria or of green *Noctiluca scintillans*, (2) surface accumulation of red *N. scintillans* (a purely heterotrophic plankton devoid of chlorophyll *a*), (3) red tides of *Mesodinium rubrum* (a phycoerythrin-bearing ciliate), (4) green seawater discolorations of *Lepidodinium chlorophorum* (a dinoflagellate with unusual carotenoids), (5) blooms dominated by a dinoflagellate such as *Prorocentrum*, *Gymnodinium*, *Lingulodinium polyedra*, *Gonyaulax* or *Alexandrium*, and (6) brown tides dominated by a dinoflagellate (such as *Karenia*, *Karlodinium veneficum*, *Protoceratium reticulatum*, *Margalefidinium polykrikoides*, or *Tripos fusus*), a prymnesiophyte (*Phaeocystis*), or a pelagophyte (*Aureococcus anophagefferens*). While the results presented here are inherently limited by the concomitant availability of in situ and S2 observations, as well as by S2 spectral resolution, it is a step forward to an improved understanding of HAB bio-optical diversity.

1. Introduction

Red tides are massive concentration of phytoplankton biomass caused by the growth and/or physically-driven accumulation of photoautotrophic, mixotrophic, or purely heterotrophic microalgae (Ryther, 1955; Smayda, 1997a), discolouring seawater with a variety of green, orange, reddish or brownish shades and hues (Dierssen et al., 2006; Siano et al., 2020). Although seemingly uncomplicated, defining a red tide is a complex task (Smayda, 1997b; Ericson, 2017; Wells et al., 2020). For the sake of simplicity, a red tide will be here defined as a

* Corresponding author.
E-mail address: pierre.gernez@univ-nantes.fr (P. Gernez).

https://doi.org/10.1016/j.rse.2023.113486
Received 24 July 2022; Received in revised form 17 January 2023; Accepted 22 January 2023
Available online 8 February 2023

massive accumulation of phytoplankton (including blooms of cyanobacteria) in the upper layer of the water column, for which the pigmented biomass is high enough to cause blatant seawater discoloration, whatever its colour (i.e. brown, red, yellow, green, etc.). Besides their esthetical annoyance, red tides are generally classified as "harmful algal blooms" (HABs) because the causative species produce toxins that accumulate in food webs and/or because the remineralization of high microalgal biomass by bacteria results in hypoxia leading to mass mortality of marine fauna (Hallegraeff, 1993). Red tides alter marine ecosystems and pose severe risks to human health, aquaculture, and food security (Anderson, 2009; Brown et al., 2020).

Red tides have been reported since historical times: several authors interpreted ancient descriptions of seawater discoloration as phytoplankton blooms, such as the red waters of the Nile river in the Bible (cited in Hallegraeff, 2003), as well as the many occurrences of "wine-like" and "purple" seawater discoloration in Homer's Odyssey (Goy, 2003). Nowadays red tides are a major concern worldwide, all the more as the HAB risk has been exacerbated by escalating eutrophication, global warming, associated poleward shift of marine species, wide-ranging spread of non-indigenous species, overall degradation of water quality and biodiversity loss that characterize modern industrial societies (Anderson, 2009; Berdalet et al., 2016; Glibert, 2017; Hallegraeff et al., 2021).

In that context, it is of the utmost importance to develop an increased understanding of the ecological processes underlying massive phytoplankton blooms (Smayda, 1997a; Wells et al., 2015, 2020), as well as to implement a global HAB monitoring system (Anderson, 2009; Anderson et al., 2019). By providing synoptic observations of radiometric changes associated with variations in seawater coloured constituents, ocean colour satellite remote sensing can document when and where red tides occur, thus making it possible to generate statistical descriptors of bloom spatial and temporal dynamics (Gower et al., 2008; IOCCG, 2021). While many remote sensing studies of high biomass blooms are available in the literature, most of them focused on one dominant species in a given case study area, such as *Karenia brevis* in the Gulf of Mexico (Carder and Steward, 1985; Stumpf et al., 2003; Tomlinson et al., 2009), *Trichodesmium* in Australian waters (McKinna et al., 2011; Blondeau-Patissier et al., 2018), *Noctiluca scintillans* in the China Sea (Qi et al., 2019), *Lingulodinium polyedra* off California (Kahru et al., 2021) and in South Africa (Pitcher et al., 2019), cyanobacteria in the Baltic Sea (Kutser et al., 2006; Kahru et al., 2007), as well as *Alexandrium monilatum*, *Prorocentrum minimum*, or other red tide species in the Chesapeake Bay (Wolny et al., 2020). Despite the relative abundance of HAB remote sensing studies over the past decades, the number of documented bloom-forming species is still very limited in comparison to the ~300 known taxa of red tide producing species (Sournia, 1995).

One reason for such a shortcoming is that accurate observation of red tides is extremely challenging in coastal areas where phytoplankton concentration can drastically change over time scales from minutes to days, and where its spatial distribution typically displays small-scale variability associated with fronts and sub-mesoscale patchiness (Gower et al., 1980; Franks, 1992; Cloern and Jassby, 2010). Satellite missions all present limitations in temporal, spatial, and/or spectral resolution when it comes to monitoring phytoplankton patches in estuaries, bays, fjords, or coastal lagoons (Blondeau-Patissier et al., 2014; Muller-Karger et al., 2018; Schaeffer and Myer, 2020). Compared to previous and current sensors, the multispectral imager (MSI) onboard the Sentinel-2 (S2) satellites has been demonstrating improved capabilities for the detection of nearshore HABs due to its ability to observe inland and coastal waters at a spatial resolution of ~20 m in 10 spectral bands from the visible to short-wave infrared spectral domains (Caballero et al., 2020). In addition, S2/MSI provides accurate measurements of the water-leaving radiance due to the development and implementation of atmospheric correction and deglinting algorithms specifically designed for optically complex coastal zones (Pahlevan et al., 2021). Despite such enhanced observation capabilities, S2/MSI has not been fully exploited for red tides observation: S2 is still poorly integrated in HAB remote sensing studies (IOCCG, 2021), and only a modicum of red tides species has been investigated so far over a limited number of regional cases (Caballero et al., 2020; Rodríguez-Benito et al., 2020; Bramich et al., 2021; Caballero and Navarro, 2021; Roux et al., 2022). A more exhaustive and broader assessment of the ability of satellite remote sensing (in general) and of S2 (in particular) to detect and discriminate red tide species is still lacking.

In that context, our main objective was to pool together, in a single study, a worldwide database of red tides detected by S2 and for which the causative species has been concurrently identified from field sampling. Such a geographically and taxonomically diverse compilation of high biomass blooms was then used to characterize the typical reflectance of as many red tides species as possible, and to identify how many optical bloom types could be discriminated from their reflectance signature. More generally, by investigating the overall relationship between the taxonomical and optical diversity of massive coastal blooms, this study aimed at providing new perspectives in HAB research using high spatial resolution satellite remote sensing.

2. Material and method

2.1. Sentinel-2 red tide database

A S2 database of highly concentrated phytoplankton blooms was compiled from a systematic search of in situ HAB events available in the harmful algae event database (HAEDAT), which contains worldwide records of harmful algal blooms since 1985 (Hallegraeff et al., 2021). The HAEDAT database was searched from 2015 to 2021 (i.e., since the start of the S2 mission) using "high phytoplankton concentration" as search criteria. From an initial set of 554 entries, a first subset of 304 events was extracted to only select the bloom records for which the causative species have been identified from microscopic analysis of field samples. The level of details provided in the selected HAEDAT dataset varied a lot from one record to another. The minimal information only contained the name of the dominant species, whereas some records included additional information on seawater discoloration, toxins, chlorophyll-*a* (Chl *a*) concentration, cell number, and/or co-occurring species.

The database of high-biomass blooms was complemented by a search of the French phytoplankton and phycotoxin monitoring network (REPHY). The REPHY is a large network of long-term time series of phytoplankton flora and toxins along the French coasts, operating since the 1980s (Belin et al., 2021). The REPHY database contains the detailed composition and abundance of microphytoplankton assemblage observed at fixed and regularly sampled stations. Phytoplankton events occurring after July 2015 were selected when a single species or genus was dominating the whole community by >85% and when its abundance was $>10^5$ cells L^{-1}.

The red tide database was complemented by the compilation of massive bloom records documented in the scientific literature (Caballero et al., 2020; Ershadifar et al., 2020; Smith and Bernard, 2020; Qi et al., 2020; Wolny et al., 2020; Caballero and Navarro, 2021; Karlson et al., 2021; Dolatabadi et al., 2021; Kahru et al., 2021; Roux et al., 2022). Results from regional monitoring reports and citizen science (e.g., Phenomer project, Siano et al., 2020) were also included. Blooms where several species co-occurred at high concentration were not selected. For example, a massive bloom observed in Chile was disregarded because two predominant dinoflagellate species (*Margalefinidum* sp. and *Lepidodinium chlorophorum*) were reported as being responsible for the seawater discoloration (Rodríguez-Benito et al., 2020), thus creating a spectral confusion between their reflectance fingerprints.

From the large list of field records preliminary gathered from the HAEDAT, REPHY, and various additional in situ observations, only bloom events synchronous to cloud-free S2 acquisitions were selected,

and limited to the cases where a phytoplankton seawater discoloration was conspicuously visible on the scene (see 2.3 for more information on the detection of bloom pixels). *In fine*, the final database was composed of bloom events for which (i) in situ information of the causative species was available, (ii) the phytoplankton assemblage was essentially dominated by one species, and (iii) resulting in obvious seawater discoloration sufficiently large to be visually identified on a concurrent cloud-free S2 observation at a spatial resolution of 20 m. From the atmospherically corrected and deglinted S2 red tide database (see 2.2), a spectral library of remote-sensing reflectance (R_{rs}) was compiled (see 2.3), and further analysed in order to evaluate S2 ability to distinguish the dominant phytoplankton genus or species in the case of highly concentrated blooms (see 2.4).

2.2. Atmospheric and glint correction of Sentinel-2 data

Level 1 (L1C) S2/MSI data were downloaded from the Copernicus open access hub. The algorithm for atmospheric correction (AC) and sunglint removal of S2-like images (GRS) was applied to L1C data (Harmel et al., 2018) after resampling at a spatial resolution of 20 m to retrieve the spectral remote-sensing reflectance, $R_{rs}(\lambda)$. GRS exploits the spectral information in the shortwave infrared (SWIR) bands where the water column is virtually black to proceed with the sunglint correction. In the case of massive cyanobacterial and *Noctiluca* blooms, which potentially produce a non-negligible signal in the SWIR bands, the glint correction was turned off. Similarly, the land mask was removed in that case to avoid flagging as "vegetation" water pixels characterized by extremely high $R_{rs}(\lambda)$ in the infrared associated with surface accumulation of floating microalgae. The performance of the GRS processing was assessed using in situ $R_{rs}(\lambda)$ match-ups specifically acquired during massive blooms (see Figs. S1–1,2 in supplementary material #1) and compared to other commonly used AC algorithms (see Table S1 in supplementary material #1). The GRS algorithm was selected because it performed very satisfactorily in the case of high biomass blooms, and contains a deglinting method that prevented the systematic masking of many bloom pixels.

2.3. Compilation of red tide spectral library

For each image of the S2 red tide database, bloom pixels were selected using a combination of visual and radiometric criteria with the objective of identifying the most concentrated phytoplankton patches. Scene features were inspected in true (RGB) and false-colour (REGB) composites using the $R_{rs}(\lambda)$ of S2 spectral bands centred at 665, 560, and 490 nm, and 705, 560 and 490 nm, respectively. The rationale for using the REGB composite with the band at 705 nm in the red channel is that a peak at the red-edge region is expected in the case of high phytoplankton biomass, thus highlighting the bloom from the background. In the case of a bloom, $R_{rs}(\lambda)$ at 665 nm is reduced due to the influence of high Chl *a* absorption, whereas $R_{rs}(\lambda)$ displayed a peak at 705 nm resulting from the interplay between particle backscattering with pure seawater and Chl *a* absorption (Gitelson, 1992). The Sentinel application platform software (SNAP) was used for image visualization by adjusting the linear stretch of each RGB or REGB band manually, thereby resulting to different settings between images. The setting of each image is detailed in the corresponding figure's legend.

A radiometric indicator, namely the normalized difference chlorophyll index (NDCI, Mishra and Mishra, 2012) was also computed to detect patches of high Chl *a* concentration. For each S2 observation, a visual analysis of the RGB, REGB, and NDCI images was performed to select 10 pixels amongst the highest patches of Chl *a* concentration, from which the averaged $R_{rs}(\lambda)$ was computed. The reason to select pixels with conspicuously high phytoplankton biomass was that the optical variability associated with non-bloom constituents (coloured dissolved organic matter (CDOM), non-algal particles (NAP), and phytoplankton species other than the predominant taxon) was minimized. The resulting spectrum was considered as the typical $R_{rs}(\lambda)$ spectrum of a given predominant phytoplankton species and/or genus observed at very high concentration during a massive bloom event. Then, all the $R_{rs}(\lambda)$ spectra were compiled to create a spectral library of S2 red tides, from which the main bloom types were discriminated and analysed.

2.4. Analysis of the red tide spectral library

The $R_{rs}(\lambda)$ spectra were standardized in order to prioritize the influence of the spectral shape during the classification process. The standardized remote-sensing reflectance was defined as:

$$R^{s}_{rs}(\lambda) = \frac{R_{rs}(\lambda) - R_{rs}(490)}{\int_{490}^{865} R_{rs}(\lambda)\, d\lambda} \quad (1)$$

Though the subtraction of $R_{rs}(490)$ modifies the reflectance shape, it was done to reduce possible bias associated with AC uncertainties, which could occur in the blue range of the visible spectrum due to variation in aerosol optical properties. Subtracting $R_{rs}(490)$ also limits the influence of varying amounts of CDOM and NAP (which are higher in this spectral range than at longer wavelengths) on the classification process. By virtue of the standardization, the variability associated with the changes in $R_{rs}(\lambda)$ amplitude (which is associated with the variation in Chl *a* concentration, as well as with varying concentrations in CDOM and NAP) was minimized, thus enabling the classification process to be mostly driven by the reflectance's spectral shape (whose variation is associated with pigments composition, phytoplankton cell size and refractive index).

When several species from the same genus were present in the spectral library, the corresponding $R_{rs}(\lambda)$ spectra were pooled together and averaged at genus level because the discrimination of the bloom-forming phytoplankter at species level is generally extremely challenging using multispectral information. Similarly, the occurrences of the same species were grouped and the species-averaged $R_{rs}(\lambda)$ was computed. Averaging the standardized $R_{rs}(\lambda)$ at species and/or genus level made it possible to reduce the phenotype variability within a single species, or the inter-specific variability within a single genus, as well as to increase the geographical and temporal robustness of the selected bloom types. In the case of blooms dominated by *Noctiluca scintillans*, the green and red forms were distinguished because the presence of a photosynthetic symbiont within the green *Noctiluca* has a significant impact on its reflectance spectral shape (Qi et al., 2019), compared to the red *Noctiluca* which is purely heterotroph and does not contain Chl *a* (Harrison et al., 2011).

A hierarchical cluster analysis (HCA) was then used to classify the bloom types into distinct optical groups using the standardized and species/genus-averaged $R_{rs}(\lambda)$ spectra as input vectors, using the dendextend package available as part of the R software for statistical computing. The eight S2 spectral bands from 490 to 865 nm were taken into account in the HCA. The SWIR spectral bands at 1610 and 2185 nm were not considered in the classification because the SWIR reflectance was not significantly different from zero in many cases. The spectral band at 443 nm was excluded in order to minimize the influence of AC uncertainties on the clustering results, and because its spatial resolution (60 m) is too low to detect small-scale features. The HCA is an unsupervised classification algorithm that partitions a given set of input data into distinct groups along a hierarchical cluster tree, which has been previously applied to cluster multispectral $R_{rs}(\lambda)$ field measurements in relation to their pigment assemblages (Torrecilla et al., 2011), or to classify hyperspectral absorption and reflectance of phytoplankton cultures into different taxonomic groups (Xi et al., 2015; Soja-Woźniak et al., 2018). The HCA method depends on the linkage algorithm used to compute the pairwise distance between the input vectors: a cosine distance was selected in the present study (Millie et al., 1997; Torrecilla et al., 2011). The distance (d) is defined as one minus the cosine of the angle between each pair of objects:

$$d(\boldsymbol{x_1},\boldsymbol{x_2}) = 1 - cos(\theta) = 1 - \frac{\boldsymbol{x_1} \bullet \boldsymbol{x_2}}{\|\boldsymbol{x_1}\| \bullet \|\boldsymbol{x_2}\|} \quad (2)$$

where the $\boldsymbol{x_1}$ and $\boldsymbol{x_2}$ vectors correspond to a pair of standardized $R_{rs}(\lambda)$ spectra at S2 spectral bands from 490 to 865 nm. In the case of two similar reflectance spectra, d equals 0. The higher the dissimilarity between the two spectra, the closer to 1 is d. The optimal number of clusters was obtained by graphically analysing the increase of the linkage distance along the nodes of the dendrogram: the point at which the distance started to stagnate corresponded to the optimal number of clusters where to cut off the classification tree, and all objects located below this point were assigned to a single cluster (Torrecilla et al., 2011). For each cluster, the mean $R^s_{rs}(\lambda)$ and its standard deviation were computed from the $R_{rs}(\lambda)$ of all bloom events caused by the species belonging to the cluster.

3. Results

3.1. Taxonomic and geographic diversity of the Sentinel-2 red tide database

From 2015 to 2021, a total of 108 bloom records were compiled in the coastal waters of 21 countries over 59 S2 tiles worldwide (Fig. 1). The location and date of each bloom event is detailed in supplementary information (suppl. material #2).

The database covered 27 taxonomic species belonging to 20 genera within 5 classes (Table 1). In terms of taxonomic diversity, the database was dominated by two classes, with *Dinophyceae* (60 bloom events) and *Cyanophyceae* (32 events) covering 85% of the bloom records. The remaining cases were distributed into three classes: *Litostomatea* (8 events), *Prymnesiophyceae* (6 events), and *Pelagophyceae* (2 events).

While the first two classes were taxonomically diverse (19 dinoflagellates species, 5 cyanobacteria genera), the other classes were only composed of one or two taxa (1 ciliate species: *Mesodinium rubrum*, 1 prymnesiophyte genus: *Phaeocystis*, and 1 pelagophyte species: *Aureococcus anophagefferens*). After averaging at species and/or genus level, a total number of 21 $R_{rs}(\lambda)$ red tide spectra was obtained, corresponding to 20 distinct taxonomically distinct genera and the two forms of *N. scintillans*.

3.2. Optical diversity of the S2 red tide database

3.2.1. Overall reflectance variability

The overall analysis of the 21 bloom spectra computed from the S2 red tide database demonstrated a high degree of variability in $R_{rs}(\lambda)$ amplitude (Fig. 2a). All $R_{rs}(\lambda)$ spectra displayed features typical of massive blooms (peak at 705 nm, e.g., Gitelson, 1992) or surface scums (sharp red-edge increase from 665 to 740 nm and high $R_{rs}(\lambda)$ plateau in the NIR from 740 to 865 nm, e.g., Spyrakos et al., 2018). For example, $R_{rs}(705)$ varied over one order of magnitude (0.007–0.063 sr^{-1}) with a mean around 0.023 sr^{-1}. Bloom events with surface scums displayed extremely high reflectance in the NIR, with $R_{rs}(788) > 0.04$ sr^{-1}. For such type of blooms, the depth of penetration was estimated to be of the order of a few tens of cm (Kutser, 2004), thus suggesting that the compiled spectral library typically represents dense surface concentration. Interestingly, blooms of the red *N. scintillans* were an exception to the general patterns: they displayed a roughly flat spectrum from 560 to 865 nm, which was consistent with previous in situ (Astoreca et al., 2005) and satellite (Qi et al., 2019) observations. Due to such a particular spectral shape, blooms of the red *N. scintillans* were characterized with a low, slightly negative or positive NDCI around 0.017 +/− 0.027 (not shown). For all other bloom events, the NDCI was high, ranging from 0.29 to 0.93, and exceeding 0.5 in 79% of the cases (not shown). Such a high range of NDCI suggested that the Chl *a* concentration typically exceeded 100 mg m^{-3} in the sampled pixels (Mishra and Mishra, 2012).

The standardization of the reflectance spectra made it possible to highlight spectral variations occurring in the visible domain (Fig. 2b). In particular, the height of the reflectance peak at 560 nm displayed a large range of variability. For example, $R^s_{rs}(560)$ ranged from 0.05 to 1.77. Such a high degree of variability in the visible range was a strong driver for the identification of optical bloom types.

3.2.2. Optical bloom types

Six optical bloom types could be determined from the 21 $R^s_{rs}(\lambda)$ spectra shown in Fig. 2b. The cluster tree first divided into two branches at a cosine distance of about 0.12; the main lower branch further diverged into two clusters at a distance of about 0.07, whereas the main upper branch eventually ramified in four clusters, whose nodes were respectively around 0.115, 0.035, and 0.015 (Fig. 3a).

The two clusters from the lower branch corresponded to blooms caused by cyanobacteria or by the dinoflagellate *Noctiluca scintillans*. They are buoyant phytoplankton species, able to accumulate at

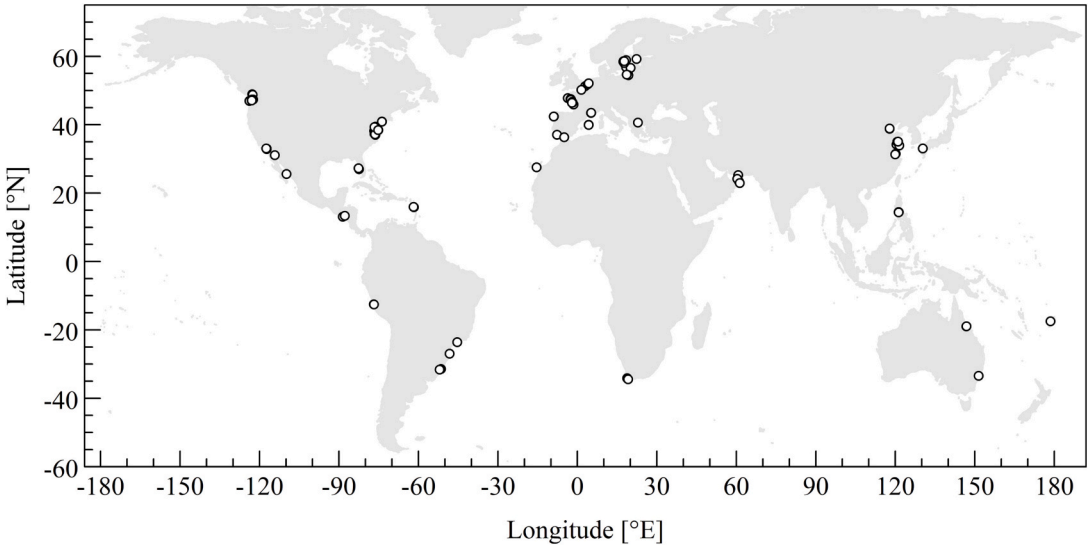

Fig. 1. Location of bloom events recorded in the Sentinel-2 red tide database.

Table 1
Phytoplankton species of the Sentinel-2 red tide database. ES = El Salvador, NL = The Netherlands, US = United States, SA = South Africa.

Class	Genus	Species	Blooms number	Countries
Dinophyceae	*Alexandrium*	*monilatum*	1	US
		ostenfeldii	2	Peru
	Gonyaulax	*digitale*	2	US
		polygramma	1	Iran
		spinifera	3	SA
	Gymnodinium	*aureolum*	1	Brazil
		catenatum	1	Mexico
		impudicum	3	France
	Karenia	*brevis*	2	US
		mikimotoi	1	Japan
	Karlodinium	*veneficum*	2	US
	Lepidodinium	*chlorophorum*	5	France
	Lingulodinium	*polyedra*	8	France, Spain, US
	Margalefidinium	*polykrikoides*	5	China, US
	Noctiluca	*scintillans* (green)	7	China, Oman
	Noctiluca	*scintillans* (red)	6	France, Greece, Spain, US
	Prorocentrum	*micans*	1	France
		minimum	4	US
	Protoceratium	*reticulatum*	3	US
	Tripos	*fusus*	2	US
Cyanophyceae	*Anabaenopsis*	sp.	5	Spain
	Aphanizomenon	sp.	8	ES, Latvia, Sweden
	Microcystis	sp.	8	Brazil, China, Philippines
	Nodularia	*spumigena*	4	Poland, Sweden
	Trichodesmium	sp.	7	Australia, Brazil, Fiji, France
Litostomatea	*Mesodinium*	*rubrum*	8	France, Iran, Mexico, Spain, US
Prymnesiophyceae	*Phaeocystis*	sp.	6	Belgium, ES, France, NL
Pelagophyceae	*Aureococcus*	*anophagefferens*	2	US

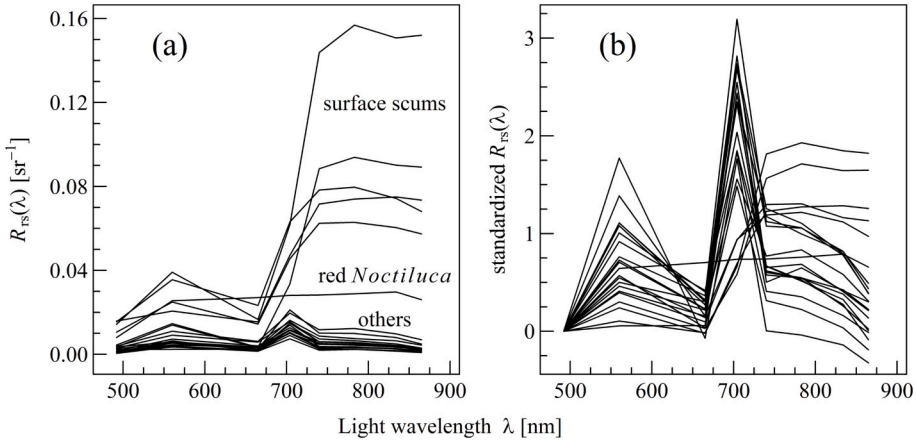

Fig. 2. Sentinel-2 red tide spectral library, showing the 21 spectra obtained after grouping the 108 bloom events at genus and/or species level (Table 1). (a) remote-sensing reflectance $R_{rs}(\lambda)$, and (b) standardized $R_{rs}(\lambda)$. The 108 reflectance spectra are shown in suppl. material #3.

extremely high concentration within a thin surface layer. Their reflectance spectrum was characterized by a high NIR plateau (Fig. 3b). Interestingly, blooms caused by the red and green forms of *N. scintillans* corresponded to distinct $R^{s}_{rs}(\lambda)$ clusters. The red *N. scintillans* composed a single optical bloom type: its $R^{s}_{rs}(\lambda)$ has a unique spectral shape, roughly constant from 560 to 842 nm. Such a particular spectral shape is consistent with previous findings (Astoreca et al., 2005; Qi et al., 2019). In contrast, the green *N. scintillans* was part of a bloom cluster dominated by scums of cyanobacteria (*Aphanizomenon* sp., *Nodularia spumigena*, *Trichodesmium* sp., and *Microcystis* sp.), whose $R^{s}_{rs}(\lambda)$ displayed the typical red-edge shape of massive phytoplankton surface accumulation, with low $R_{rs}(\lambda)$ at 665 nm and high $R_{rs}(\lambda)$ from 705 to 865 nm. Such a characteristic red-edge shape has been previously reported by Qi et al. (2020) for the green *N. scintillans* and floating cyanobacteria such as *Trichodesmium* sp., and *Microcystis* sp.

The four optical bloom types of the upper branch were all characterized by a $R_{rs}(\lambda)$ peak at 705 nm (Fig. 3c), a spectral feature characteristic of highly-concentrated phytoplankton patches (Gitelson, 1992).

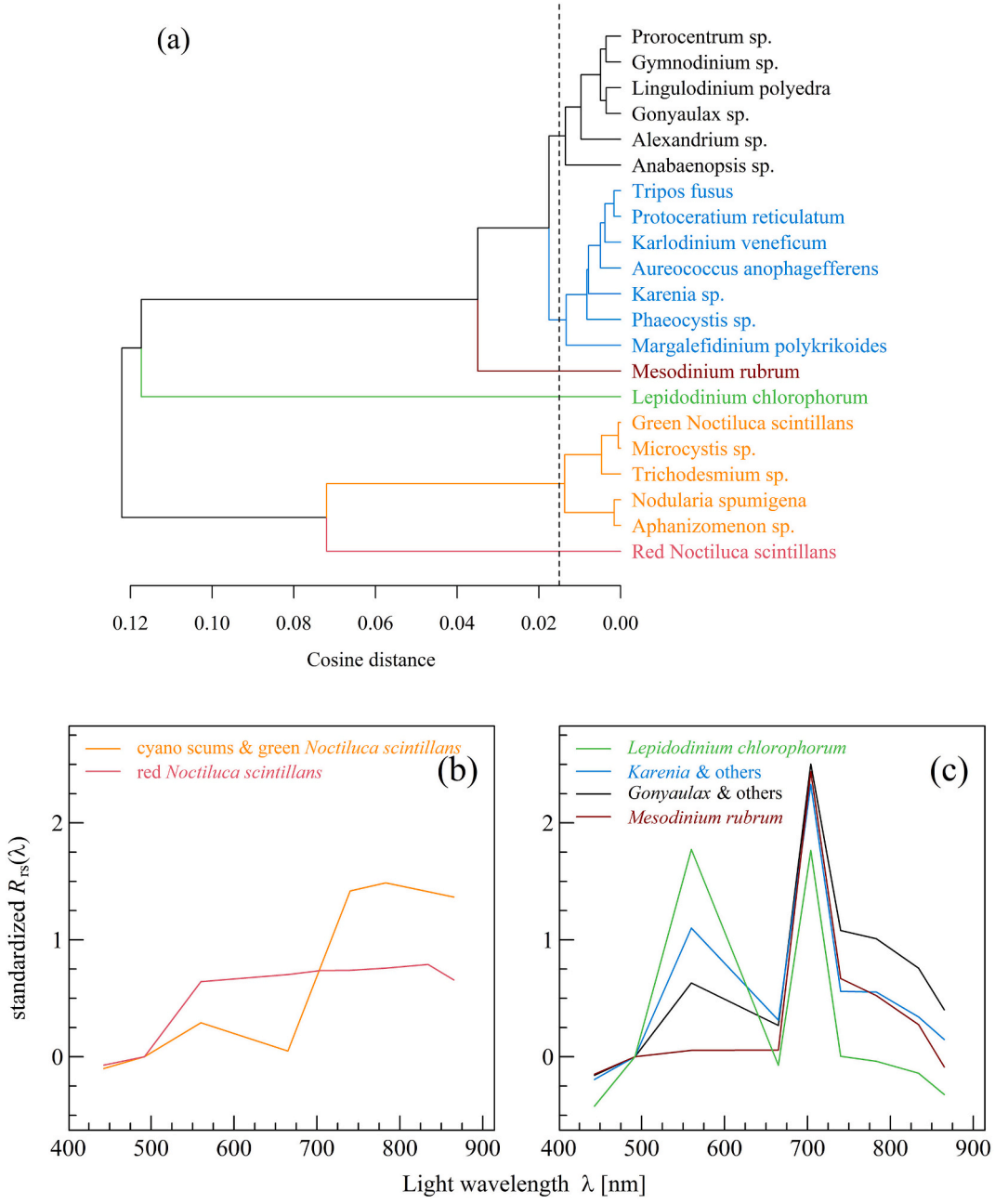

Fig. 3. (a) Cluster tree obtained using the 21 standardized $R_{rs}(\lambda)$ spectra of the S2 red tide spectral library. The cut-off distance is shown with a vertical dashed line. (b, c) Cluster-averaged spectra of the 6 optical bloom types. (For interpretation of the references to colour in this figure legend, the reader is referred to the web version of this article).

The reflectance spectra of these clusters however significantly differed in the visible spectral domain. Red tides caused by the ciliate *Mesodinium rubrum*, which corresponded to a single cluster, were characterized by a very low $R_{rs}(\lambda)$ in the green spectral region (Fig. 3c), as previously observed in situ by Guzmán et al. (2016) when sampling a red tide of the same species. The absence of a green reflectance peak was unique to the *M. rubrum* bloom cluster.

Another monospecific optical bloom type was constituted by *Lepidodinium chlorophorum*. The reflectance spectrum of this dinoflagellate was characterized by an extremely high peak at 560 nm (Fig. 3c), a spectral feature previously observed for that species using satellite remote sensing (Sourisseau et al., 2016).

Contrary to the *M. rubrum* and *L. chlorophorum* monospecific clusters, the two remaining optical bloom types were taxonomically very diverse. The shape of their reflectance spectra was also characterized by a peak at 560 nm, though of lesser amplitude than for the *L. chlorophorum* bloom type (Fig. 3c). The cluster with the lower green reflectance peak was mostly composed of dinoflagellates belonging to the following genera and/or species: *Prorocentrum*, *Gymnodinium*, *Lingulodinium polyedra*, *Gonyaulax*, and *Alexandrium* (Fig. 3a). This cluster was constituted by 5 dinoflagellate genera out 6, and it also contained the reflectance spectrum of blooms dominated by cyanobacteria from the genus *Anabaenopsis*. The last cluster was also dominated by dinoflagellates, which represented 5 of the 7 taxa: *Protoceratium reticulatum*, *Tripos fusus*, *Karlodinium veneficum*, *Karenia* sp., and *Margalefidinium polykrikoides* (Fig. 3a). This cluster also included blooms caused by a pelagophyte (*Aureococcus anophagefferens*) or by a prymnesiophyte (*Phaeocystis*).

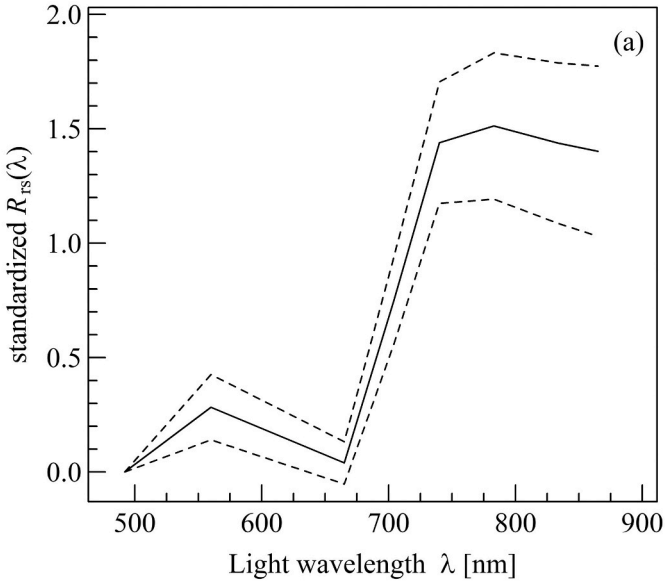

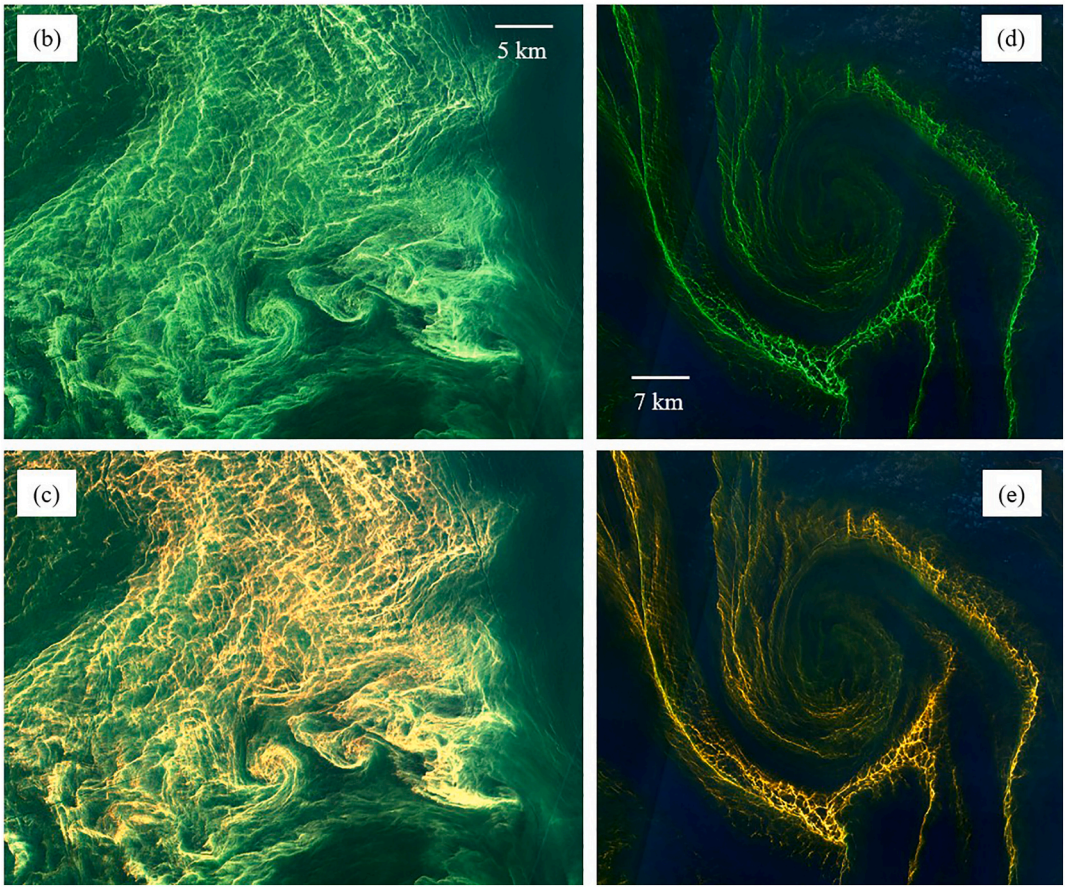

Fig. 4. Optical bloom type composed of cyanobacteria (*Microcystis* sp., *Trichodesmium* sp., *Nodularia spumigena*, and *Aphanizomenon* sp.) and of the green *Noctiluca scintillans*. (a) Averaged (+/− standard deviation) standardized $R_{rs}(\lambda)$ spectrum computed from the representative spectra of 34 red tides recorded in Australia, Brazil, China, El Salvador, Fiji, Guadeloupe, Latvia, Oman, Philippines, Poland, and Sweden. Sentinel-2 examples of a bloom of *Aphanizomenon* sp. in Sweden, 20 July 2019 (b, c), and of green *N. scintillans* in the Oman Sea, 14 March 2019 (d, e). The same image is either displayed using a RGB (b, d) or a REGB (c, e) false colour composite. The colour histogram was uniformly adjusted as follow: 0.01 sr^{-1} for all bands. (For interpretation of the references to colour in this figure legend, the reader is referred to the web version of this article).

3.2.3. *Visual appearance of the optical bloom types*

To better appraise the spectral variability of clusters as well as the resulting diversity in associated bloom colours, several representative examples of S2 images are now described for each optical bloom type (the images off all red tides are provided in suppl. material #3). Surface scums of floating cyanobacteria such as *Aphanizomenon* sp. exhibited bright green colours when displayed using a standard RGB composite (Fig. 4b); they appeared golden bright when using a false REGB

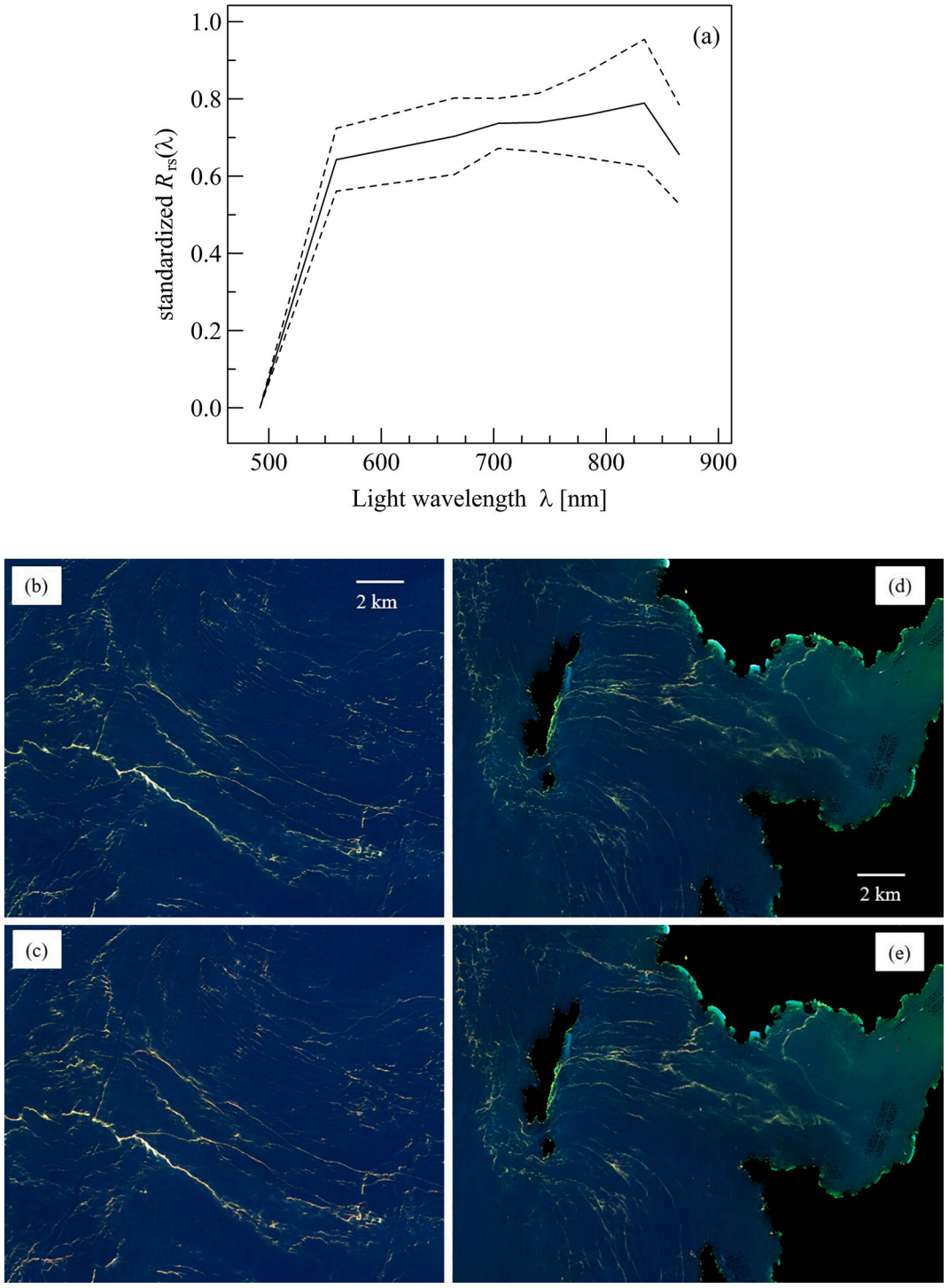

Fig. 5. Optical bloom type composed of red *N. scintillans*. (a) Averaged (+/− standard deviation) standardized $R_{rs}(\lambda)$ spectrum computed from the representative spectra of 6 red tides recorded in France, Greece, Spain, and the US. Sentinel-2 examples of red *N. scintillans* blooms in Spain off Gran Canaria Island, 13 April 2016 (b, c) and in the Ria de Vigo, 4 September 2021 (d, e). The same image is either displayed using a RGB (b, d) or a REGB (c, e) false colour composite. The colour histogram was uniformly adjusted as follow: 0.01 sr^{-1} for all bands. (For interpretation of the references to colour in this figure legend, the reader is referred to the web version of this article).

composite (Fig. 4c). Cyanobacteria blooms dominated by *N. spumigena* or *Microcystis* sp. had a similar visual appearance. On the contrary blooms of *Trichodesmium* had a different colour: they appeared dark green and reddish on the RGB and REGB images, respectively (supplementary material). Apart from the particular case of *Trichodesmium* red tides, surface aggregations of floating cyanobacteria could be confused with blooms of green *N. scintillans* due to similarity in their reflectance shape (Fig. 4a), spatial features, and visual appearance (Fig. 4d, e). Interestingly, surface aggregations of red *N. scintillans* could not be confused with blooms of other buoyant microalgae: their unique, nearly flat reflectance shape (Fig. 5a), made them appear similarly golden bright on both RGB and REGB composites (Fig. 5b-d).

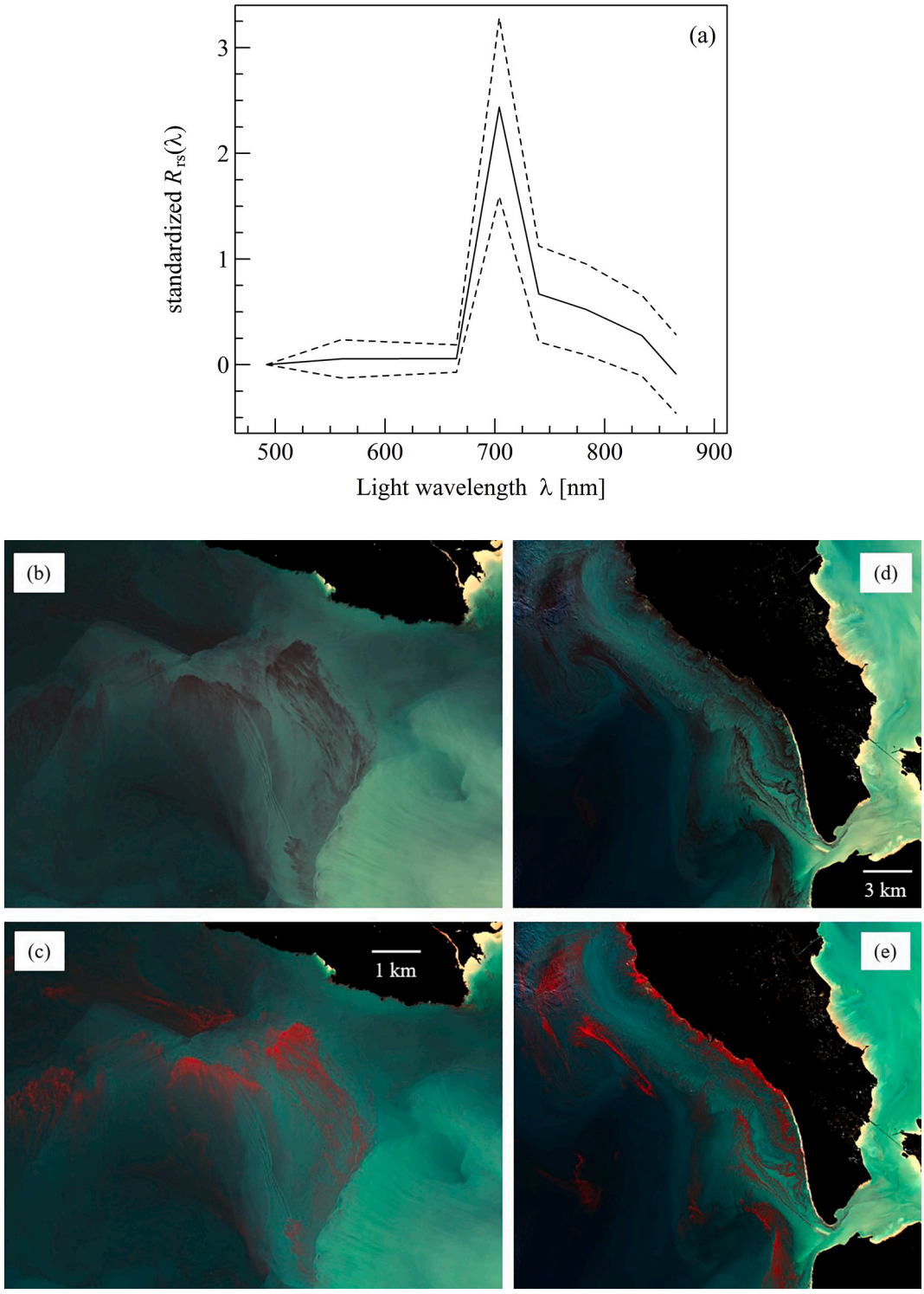

Fig. 6. Optical bloom type composed of *M. rubrum*. (a) Averaged (+/− standard deviation) standardized $R_{rs}(\lambda)$ spectrum computed from the representative spectra of 8 red tides recorded in France, Iran, Mexico, Spain, and the US. Sentinel-2 examples of *M. rubrum* red tides in France off the Loire River estuary, 12 April 2017 (b, c) and Oléron Island, 18 April 2020 (d, e). The same image is either displayed using a RGB (b, d) or a REGB (c, e) false colour composite. The colour histogram was uniformly adjusted as follow: 0.02 sr^{-1} for the red or NIR band, and 0.03 sr^{-1} for the green and blue bands. (For interpretation of the references to colour in this figure legend, the reader is referred to the web version of this article).

The other phytoplankton blooms were generally better highlighted on REGB composites than on standard RGB displays (Figs. 6-9). This was particularly obvious in the case of *M. rubrum* red tides, which constituted a monospecific cluster due to its unique reflectance shape and visual appearance (Fig. 6). Compared to the other optical bloom types, $R_{rs}(560)$ was extremely low in all investigated blooms of *M. rubrum* (the standardized reflectance was 0.06 +/− 0.18, Fig. 6a). Blooms from this ciliate therefore appeared dark burgundy red on RGB images (Fig. 6b, d) and vivid ruby red on REGB false composites (Fig. 6c, e).

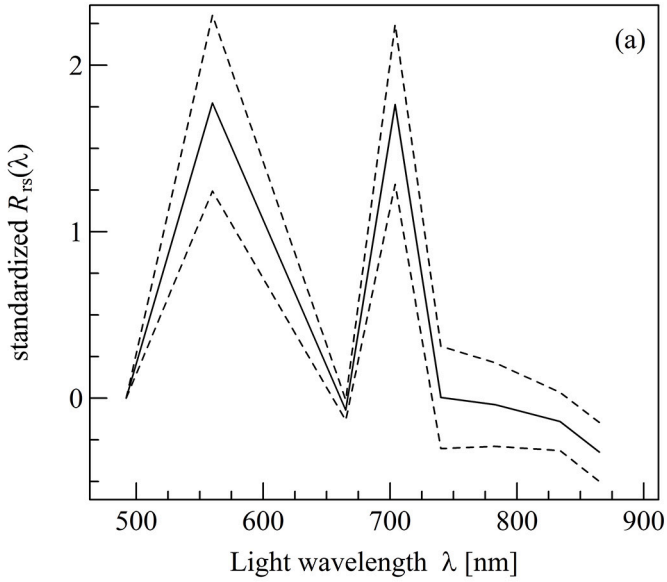

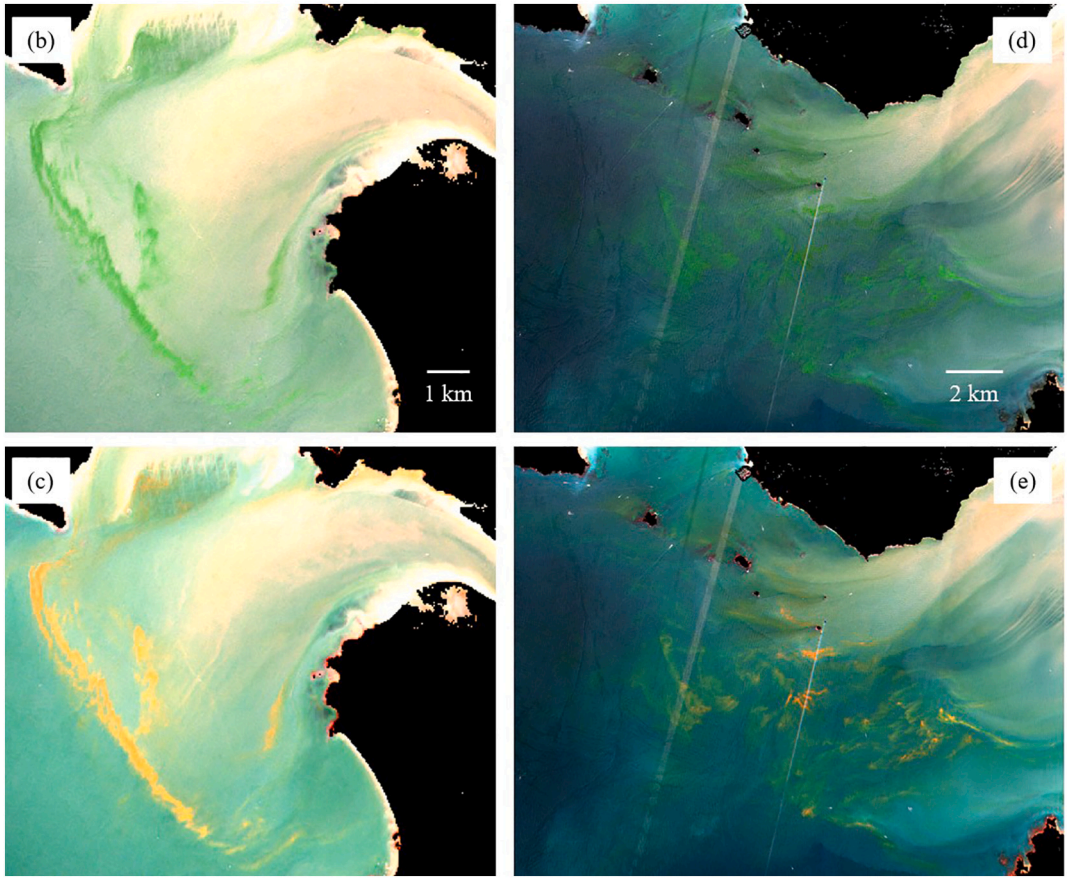

Fig. 7. Optical bloom type composed of *L. chlorophorum*. (a) Averaged (+/− standard deviation) standardized $R_{rs}(\lambda)$ spectrum computed from the representative spectra of 5 red tides recorded in France. Sentinel-2 examples of *L. chlorophorum* green seawater discoloration in France off the Vilaine (b, c) and Loire River estuaries (d, e), 21 July 2019. The same image is either displayed using a RGB (b, d) or a REGB (c, e) false colour composite. The colour histogram was uniformly adjusted as follow: 0.01 sr^{-1} for the red or NIR band, 0.02 sr^{-1} for the green band, and 0.015 sr^{-1} for the blue band. (For interpretation of the references to colour in this figure legend, the reader is referred to the web version of this article).

Contrary to *M. rubrum*, blooms of *L. chlorophorum* were conspicuous on both RGB and REGB image composites, respectively appearing brilliant green or orange, due to the extremely high green $R_{rs}(\lambda)$ peak that characterized this cluster (Fig. 7). This is the sole optical bloom type for which the standardized $R_{rs}(\lambda)$ at the 705 and 560 nm peaks had a similar magnitude (respectively 1.76 +/− 0.48, and 1.77 ±0.53, in average).

The visual appearance and reflectance spectral shape of the last two clusters, both of them dominated by dinoflagellates, were quite comparable (Figs. 8 and 9). Both types of blooms appeared murky green and/or brownish on the RGB image, and in rusty orange with reddish hues on the

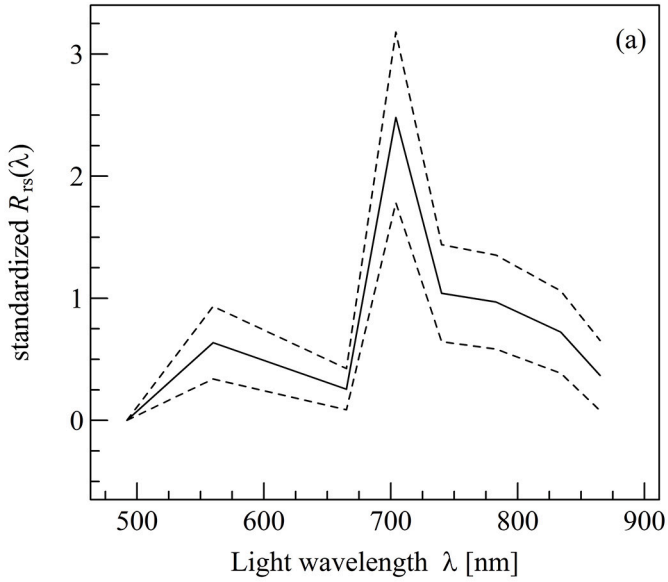

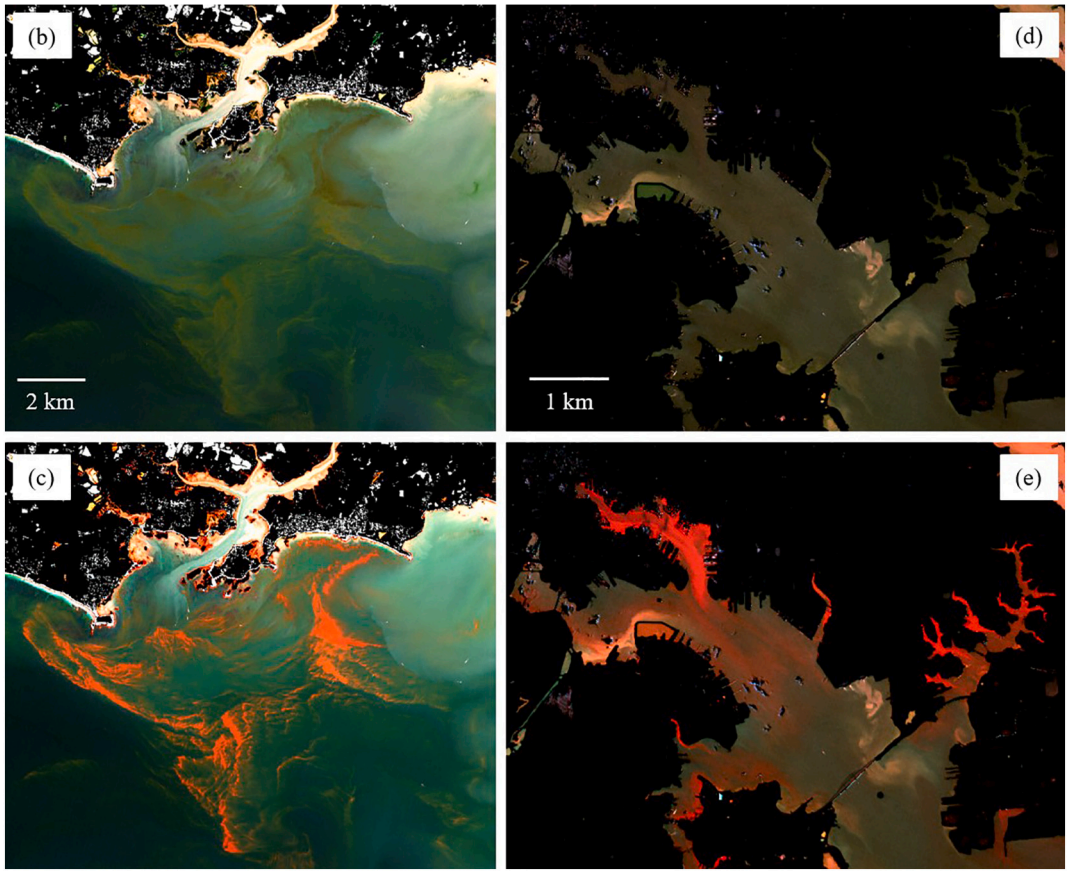

Fig. 8. Optical bloom type composed of *Prorocentrum* sp., *Gymnodinium* sp., *Lingulodinium polyedra*, *Gonyaulax* sp., *Alexandrium* sp., and *Anabaenopsis* sp. (a) Averaged (+/− standard deviation) standardized $R_{rs}(\lambda)$ spectrum computed from the representative spectra of 32 red tides recorded in Brazil, France, Iran, Mexico, Peru, South Africa, Spain, and the US. Sentinel-2 examples of a bloom of *L. polyedra* off the Vilaine River estuary (France), 14 August 2021 (b, c), and of *P. minimum* in the Chesapeake Bay (US), 16 January 2020 (d, e). The same image is either displayed using a RGB (b, d) or a REGB (c, e) false colour composite. The colour histogram was uniformly adjusted as follow: 0.01 sr^{-1} for the red or NIR band, 0.02 sr^{-1} for the green band, and 0.015 sr^{-1} for the blue band. (For interpretation of the references to colour in this figure legend, the reader is referred to the web version of this article).

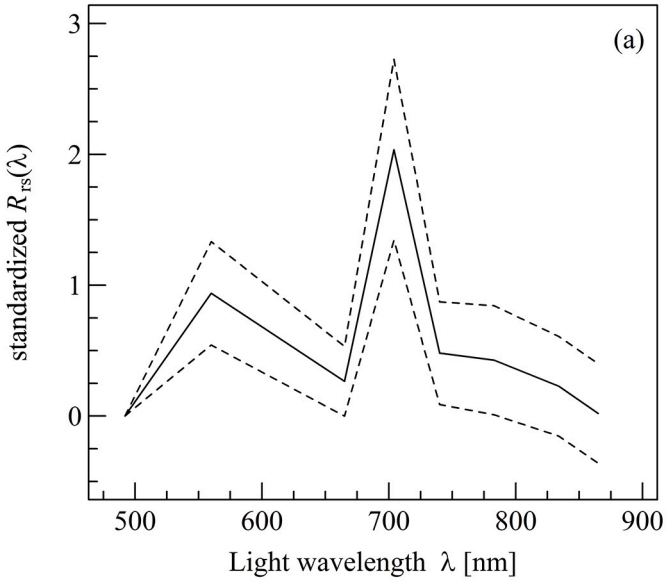

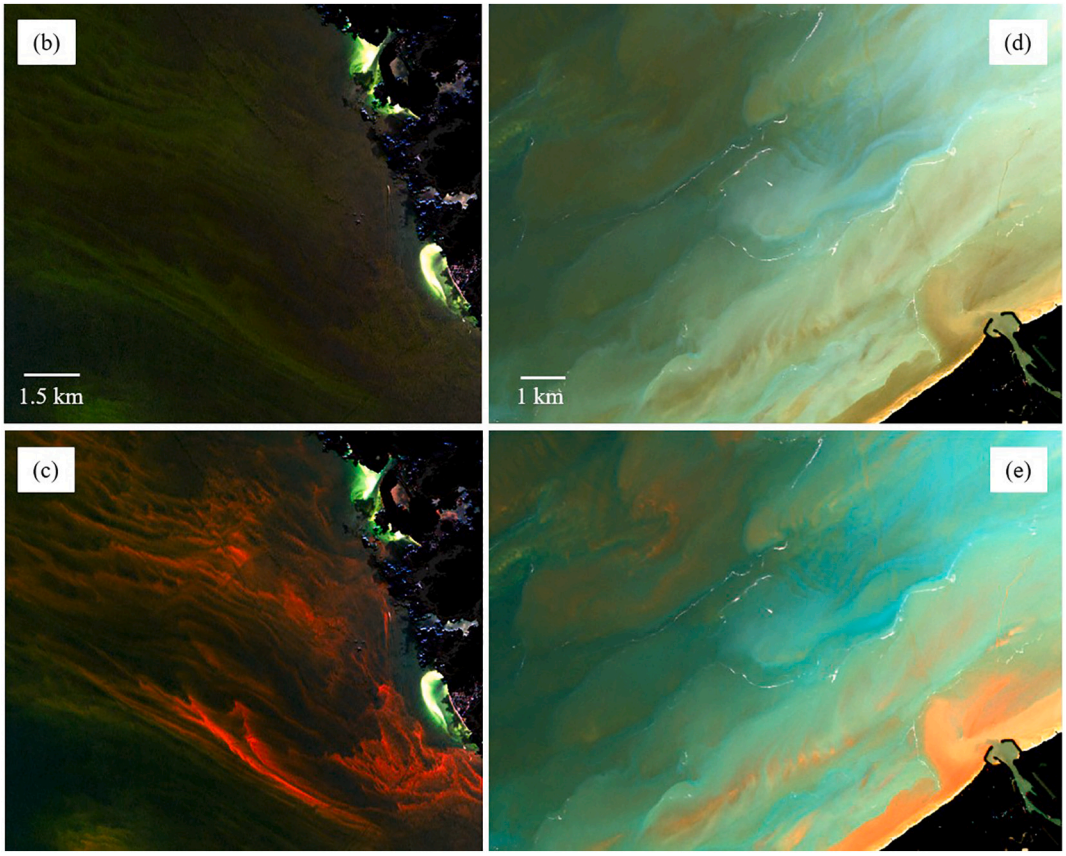

Fig. 9. Optical bloom type composed of *Protoceratium reticulatum*, *Tripos fusus*, *Karlodinium veneficum*, *Aureococcus anophagefferens*, *Karenia* sp., *Phaeocystis* sp., and *Margalefidinium polykrikoides*. (a) Averaged (+/− standard deviation) standardized $R_{rs}(\lambda)$ spectrum computed from the representative spectra of 23 red tides recorded in Belgium, China, El Salvador, France, The Netherlands, Japan, and the US. Sentinel-2 examples of a bloom of *K. brevis* off Florida (US), 7 August 2018 (b, c) and of *Phaeocystis* sp. in Belgium, 1 May 2016 (d, e). The same image is either displayed using a RGB (b, d) or a REGB (c, e) false colour composite. The colour histogram was uniformly adjusted as follow: 0.01 sr^{-1} for the red or NIR band, 0.02 sr^{-1} for the green band, and 0.015 sr^{-1} for the blue band. (For interpretation of the references to colour in this figure legend, the reader is referred to the web version of this article).

REGB composite. Despite some differences in the cluster-averaged reflectance spectra (Fig. 3c), a risk of confusion exists between these two bloom optical types. In particular, the standardized $R_{rs}(560)$ was of the same order of magnitude in both cases: 0.64 (+/− 0.30) for one bloom type (Fig. 8a) and 0.95 (+/− 0.38) for another (Fig. 9a).

4. Discussion

The present study demonstrated the ability of Sentinel-2 to detect highly concentrated harmful algal blooms. We recommend including S2 observations in HAB monitoring programs in complement to in situ

sampling (or in the worst case scenario to supply the absence of field measurements), in order to better document phytoplankton dynamics (Roux et al., 2022) as well as to provide near-real time information on red tide extent to coastal stakeholders working in aquaculture, fisheries, tourism, or other industry related to water quality (Caballero et al., 2022; Rodríguez-Benito et al., 2020). The S2 red tide database captured a wide range of phytoplankton diversity, bloom colours, spatial features, and reflectance spectral shapes (see Figs. 4-9, and suppl. material #3). The many shades of red, green, orange, yellow, and brown tides confirmed the variegated nature of seawater discoloration associated with algal blooms worldwide (Hallegraeff et al., 2021; Siano et al., 2020). To our knowledge, this is the first time that so many phytoplankton blooms were documented together in a single study at such spatial resolution. As such, it provides new insights and opens new perspectives to study highly concentrated phytoplankton blooms, as discussed in the next sections.

4.1. Ecological significance of the bloom clusters

4.1.1. Influence of biomass: blooms of buoyant cyanobacteria and Noctiluca

The classification of the $R_{rs}(\lambda)$ dataset into bloom optical types was primarily driven by two factors: changes in biomass, and changes in pigments composition. The overall spectral shape of the cyanobacteria and green *N. scintillans* bloom cluster (Fig. 3b, and Fig. 4a) was caused by the dense accumulation of microalgae within a thin surface layer. For that optical bloom type, $R_{rs}(\lambda)$ exhibited a high NIR plateau typical of floating microalgae (Qi et al., 2020) and $R^{s}_{rs}(\lambda)$ was consistent with the optical water type described as "hypereutrophic waters with scum of cyanobacterial bloom and vegetation-like $R_{rs}(\lambda)$" in Spyrakos et al. (2018). It is noteworthy that such a notable $R_{rs}(\lambda)$ shape was related to specific traits such as the ability to form floating colonies or filaments, or to a distinctive cellular structure, namely the presence of buoyant gas vacuoles. Such ecological / morphological characteristics were common to all species from this cluster. Indeed, *Nodularia spumigena* and *Aphanizomenon flosaquae* are amongst the most common filamentous bloom-forming cyanobacteria of the Baltic Sea (Karlson et al., 2021), the colonial *Microcystis* is a cosmopolitan bloom-forming cyanobacterium (Harke et al., 2016), and bloom reports of the filamentous *Trichodesmium* appeared in the expedition logs of Charles Darwin and James Cook (cited in Capone, 2021) as well as in Jules Verne's famous novel "20,000 leagues under the sea" (cited in Bergman et al., 2013). Interestingly, the high NIR reflectance cluster composed of floating phytoplankton was not limited to cyanoblooms; it also contained surface accumulation of a vacuolated dinoflagellate, namely the green *N. scintillans*. While being heterotrophic, *N. scintillans* can harbour a photosynthetic green flagellate symbiont in warm waters (Elbrächter and Qi, 1998), thus explaining the radiometric affinities between cyanoblooms and surface aggregation of green *N. scintillans* (Fig. 4a), as previously reported in Qi et al. (2019, 2020). From an optical point of view, the reflectance NIR plateau likely resulted from (i) the extremely high backscattering coefficient of buoyant vacuolated species such as *N. scintillans*, *Trichodesmium*, and *Microcystis* (Astoreca et al., 2005; Dupouy et al., 2008; Moore et al., 2017; Qi et al., 2020), and/or (ii) the negligible role of water column absorption in a dense layer of microalgae accumulated on top of the water surface, as typically observed for cyanoblooms (Quibell, 1992; Kutser, 2004; Matthews et al., 2012).

The other cluster composed of surface aggregation of floating phytoplankton was monospecific, and consisted in "blooms" of red *N. scintillans*. In the absence of photosynthetic symbiont, surface accumulations of *N. scintillans* generally appear reddish or orange in temperate waters (Elbrächter and Qi, 1998). Our results confirmed that surface accumulations of red *N. scintillans* could be fingerprinted by satellite imagery due to their unique optical properties (Qi et al., 2019). The unique spectral shape of the red *N. scintillans* cluster (Fig. 5a) was presumably determined by a very particular absorption coefficient associated with a specific pigment composition, mainly constituted of carotenoids and almost completely deprived of chlorophylls (Balch and Haxo, 1984). The lack of $R_{rs}(\lambda)$ valley at 665 nm was therefore very likely due to the absence of chlorophyll *a*. From a practical point of view, such results demonstrate that standard red-edge algorithms are not designed to detect surface aggregation of red *N. scintillans*. Specific algorithms, which do not depend on Chl *a* optical properties, are instead required (Qi et al., 2019). While being unique due to its atypical pigment composition and conspicuous reflectance shape, the red *N. scintillans* optical bloom type also consists in a remarkable ecological case of surface accumulation by purely heterotrophic phytoplankton.

Contrary to the cyanobacteria and *N. scintillans* bloom clusters, the spectral shape of the four other optical bloom types (Fig. 3c, and Figs. 6-9) was primarily driven by the variability in pigments composition. Differences in phytoplankton biomass obviously occurred between the blooms compiled here, but such changes likely contributed at second order to the overall variability of the standardized $R_{rs}(\lambda)$ spectra. Besides the red *N. scintillans* cluster, which is optically unique due to the lack of Chl *a*, two other monospecific optical bloom types were related to a particular pigment composition: red tides of the ciliate *M. rubrum*, and green seawater discolorations of the dinoflagellate *L. chlorophorum*. The bloom clusters primarily driven by changes in pigment composition are discussed in the next sub-sections.

4.1.2. Influence of pigments type: phycoerythrin and M. rubrum red waters

The conspicuous dark burgundy colour of *M. rubrum* red tides has been encountered at sea for long. Early records include reports of red waters off Chile by Darwin during the Beagle voyage (Darwin, 1839), in Iceland in the early 1900s (Paulsen, 1909 cited in Hart, 1943), or around Cape Peninsula in South Africa (Hart, 1934). Blooms of *M. rubrum* have then been frequently documented in coastal waters worldwide (Ryther, 1967; Fenchel, 1968; Crawford, 1989; Herfort et al., 2011). The geographic diversity of the events collated in the present study (including bloom reports in France, Iran, Mexico, Spain, and the US) confirmed the worldwide occurrence of *M. rubrum* red tides (Table 1). For all these events, the dark red coloration can be non-ambiguously attributed to the presence of phycoerythrin (PE) within this ciliate (Gustafson et al., 2000). Indeed, the particular pigment composition of *M. rubrum* (Zapata et al., 2012; Rial et al., 2013) explains the unique visual aspect and spectral shape of the corresponding optical bloom type, with the low $R_{rs}(\lambda)$ around 490, 560, and 665 nm being due to the absorption by Chl c_2 and alloxanthin, PE, and Chl *a*, respectively (Fig. 10a).

M. rubrum is a kleptoplast mixotrophic ciliate able to functionally use the chloroplasts acquired during the ingestion of phycobiliprotein-bearing cryptophytes such as *Teleaulax* sp. (Yih et al., 2004). For that reason, the resulting dark burgundy red tides could be caused by a dominance of the ciliate or of its prey, as well as by the co-occurrence of both species in high concentration (Johnson et al., 2013; Yih et al., 2013). Furthermore, mixotrophic dinoflagellates from the *Dinophysis* genus being obligate feeders of *M. rubrum* (Park et al., 2006), they also have a cryptophyte-like pigment composition (Rial et al., 2013). While *Dinophysis* is generally found at low concentration (Reguera et al., 2012) even during "high" events (Díaz et al., 2021), exceptional blooms dominated by this dinoflagellate have been previously reported (e.g., Mafra et al., 2019). In the present study, the phytoplankton biomass of the selected red water events was dominated by *M. rubrum* (Souchu et al., 2017; Conejo-Orosa et al., 2019; Ershadifar et al., 2020). Nevertheless, if captured by Sentinel-2, red tides dominated by *Teleaulax* sp. and/or *Dinophysis* sp. would probably have a reflectance fingerprint similar to that of the *M. rubrum* bloom cluster.

4.1.3. Influence of pigments type: unusual carotenoid composition and L. chlorophorum green waters

The vivid green appearance of seawater discoloration caused by the bloom-forming dinoflagellate *L. chlorophorum* (Elbrächter and Schnepf,

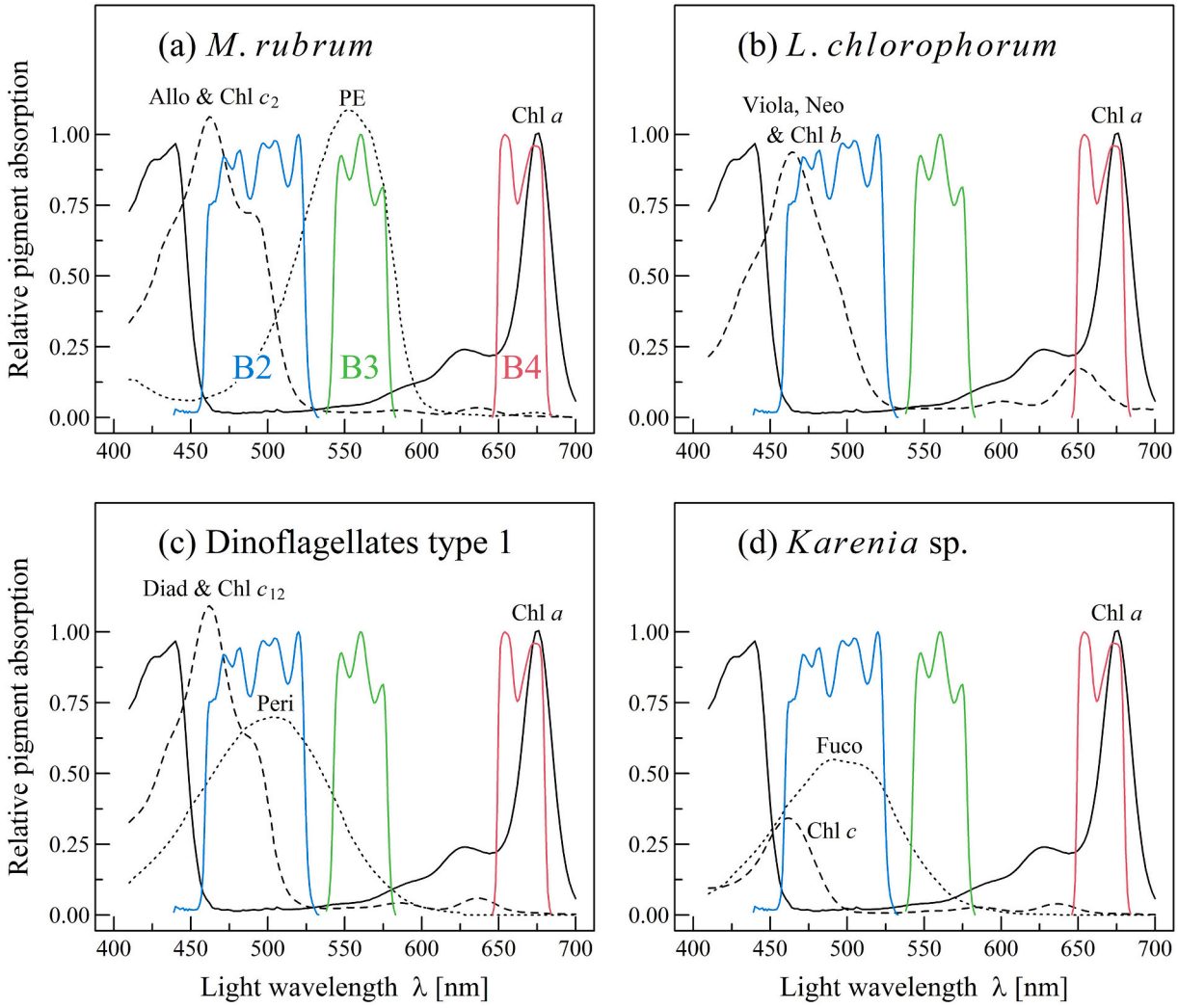

Fig. 10. Position of S2A/MSI spectral response function for the bands B2, B3, and B4, and absorption characteristics of the main pigments present in *M. rubrum* (a), *L. chlorophorum* (b), peridin-bearing dinoflagellates (c), and *Karenia* sp., as an example of fucoxanthin-bearing dinoflagellate (d). The proportion of pigments relative to Chl *a* was taken from Zapata et al. (2012). The pigment absorption data (Bricaud et al., 2004; Clementson and Wojtasiewicz, 2019) was standardized to Chl *a* absorption at 675 nm. The PE absorption data was obtained from laboratory culture of the cryptophyte *Teleaulax amphioxeia* available at Ifremer Nantes.

1996) have been frequently observed in coastal areas (Sournia et al., 1992; Siano et al., 2020; Roux et al., 2022). The high $R_{rs}(\lambda)$ peak around 560 nm characterizing *L. chlorophorum* bloom cluster (Fig. 7a) is attributable to a particular pigment composition, unique within the diversity of Dinophyceae chloroplast types (Zapata et al., 2012). Due to the absence of common carotenoids such as peridin (a biomarker pigment for dinoflagellates) or fucoxanthin (also present in some dinoflagellates, and a biomarker pigment for diatoms), the amplitude of pigment absorption in *L. chlorophorum* is very low in the 530–600 nm range (Fig. 10b). Beside Chl *a*, the main pigments of this species have absorption maxima around 465 nm (Chl *b*, violaxanthin, and neoxanthin) and 650 nm (Chl *b*), and do not absorb in the green spectral range. Altogether, such unusual pigment composition results in extremely high $R_{rs}(\lambda)$ around 560 nm, a spectral feature previously proposed as a radiometric marker for *L. chlorophorum* green seawater discoloration (Sourisseau et al., 2016).

4.1.4. Influence of pigments type: peridinin, fucoxanthin, and other bloom clusters

The last two optical bloom types produced the same kind of visual appearance and $R_{rs}(\lambda)$ spectral shape (Figs. 8, 9). Though the corresponding red tide species have different pigment types, they have similar pigments absorption properties, and could not be discriminated at the spectral resolution of S2/MSI (Fig. 10c,d). One optical bloom type is dominated by peridin-bearing dinoflagellates (*Prorocentrum*, *Gymnodinium*, *Lingulodinium polyedra*, *Gonyaulax*, and *Alexandrium*) belonging to Type 1 pigment group (sensu Zapata et al., 2012), whereas the other cluster contains peridin-bearing dinoflagellates (*Tripos fusus, Protoceratium reticulatum*, and *Margalefidinium polykrikoides*) as well as fucoxanthin-bearing species such as the dinoflagellates *Karenia* sp. and *Karlodinium veneficum*, the pelagophyte *Aureococcus anophagefferens*, and the prymnesiophyte *Phaeocystis*. Whatever the pigment type, however, their carotenoids have a broad absorption range from 400 to 600 nm (with a maximum around 505 nm for peridinin (Fig. 10c), and around 490 nm for fucoxanthin (Fig. 10d)), which explain why the reflectance of these two optical bloom types are characterized by a moderately high $R_{rs}(\lambda)$ peak at 560 nm (compared to the extremely high green peak of the *L. chlorophorum* blooms).

4.1.5. Reflectance clusters and harmful nature of phytoplankton blooms

Phytoplankton blooms could be harmful for several reasons: they produce toxins, cause damage to respiratory mechanisms of marine species (e.g., fish gills), and/or lead to oxygen depletion and ecosystem disruption (Lassus et al., 2016). While the harmful effect of a given

phytoplankton bloom, if any, can be assessed using field observation only, it is interesting to point out here an unexpected association between the $R_{rs}(\lambda)$ clusters and the harmful nature of the investigated red tides. Three optical clusters were clearly associated with toxin-producing phytoplankton species. Within the cluster composed of floating microalgae, cyanobacteria such as *N. spumigena*, *Aphanizomenon*, and *Microcystis* can produce hepato-, neuro-, and/or cytotoxins (Harke et al., 2016). The cluster dominated by dinoflagellates included toxin-producing species such as paralytic shellfish poisoning (PSP) by *Gymnodinium* and *Alexandrium*, and yessotoxin (YTX) by *L. polyedra* and *Gonyaulax* (Karlson et al., 2021). The last cluster included fish killer species (*Phaeocystis*, *Karlodinium veneficum*, and *Karenia mikimotoi*) and *K. brevis*, a dinoflagellate able to produce harmful neurotoxin (Landsberg et al., 2009).

On the contrary, the monospecific bloom optical types were constituted by species which do not produce toxins (e.g., *L. chlorophorum*, *M. rubrum*, and the red *N. scintillans*). However, blooms of *L. chlorophorum* can result in hypoxia events leading to fish and shellfish mortality (Sournia et al., 1992), presumably associated with the large amount of transparent exopolymer particles (TEP) produced by this green dinoflagellate (Roux et al., 2021, 2022). Interestingly, as red tides of *M. rubrum* can be followed by diarrhetic shellfish poisoning (DSP) outbreaks caused by the subsequent growth of *Dinophysis* (Harred and Campbell, 2014), the unique $R_{rs}(\lambda)$ signature of the ciliate red tides could be useful to develop a *Dinophysis* early-warning system. While our study opened original perspectives for a remote estimation of the harmful nature of some phytoplankton blooms, a more systematic assessment of the optical properties of harmful vs. non-harmful phytoplankton species is however required for further developments.

4.2. Current limitations and perspectives for red tide remote sensing

4.2.1. Range of applicability of the optical bloom types

The main objective of the present study was to characterize the reflectance diversity of highly concentrated phytoplankton blooms essentially dominated by a single species. Even though massive blooms are not to be strictly considered as natural analogues of culture populations, they are as close as possible to a monospecific bloom endmember (Carder and Steward, 1985). The $R_{rs}(\lambda)$ spectra compiled in the S2 red tide database were deliberately selected from pixels where phytoplankton concentration was as high as possible (based on $R_{rs}(\lambda)$ variation), in order to limit the influence of other suspended coloured constituents. Importantly, the subtraction of $R_{rs}(490)$ during the reflectance standardization (Eq. (1)) improved the consistency of the classification into optical bloom types because it limited the influence of AC uncertainties as well as of CDOM and NAP variability on the clustering process. Furthermore, by focusing on pixels displaying the reflectance characteristics of high surface concentration (i.e., $R_{rs}(\lambda)$ peak at 704 nm and/or high NIR $R_{rs}(\lambda)$), the extracted spectra are more likely to unambiguously represent the bloom in its maximum expression. The selection of a reflectance spectrum typical of dense surface accumulation, with reduced water column interferences, was facilitated by Sentinel-2 high spatial resolution (20 m). Though fine-scale patchiness is a typical feature of phytoplankton spatial distribution (e.g., Montagnes et al., 1999; Bulit et al., 2004), the risk of sampling horizontally mixed and/or vertically diluted pixels was minimized due to S2 high resolution. As such, the cluster-averaged $R_{rs}(\lambda)$ spectra identified in the present study could not be used outside the particular case of massive phytoplankton blooms, observed in a patch of high surface concentration, for which the NDCI is typically higher than ~0.3 (with the exception of red *N. scintillans* surface accumulation). With these limitations in mind, our results may help recognizing blooms in future studies: the standardized reflectance of highly concentrated pixels from an unidentified seawater discoloration can be compared with the endmember spectra of the optical bloom types shown in Fig. 3 and provided in Table 2, and eventually associated with the optical cluster showing the lowest cosine distance. This could help "tagging" red tides in the absence of in situ information: if the most concentrated patches of a bloom can be identified, then it can be linked to the rest of the red tide.

While the approach developed here is not directly compatible with the lower spatial resolution of ocean colour satellite sensors such as SeaWiFS (1 km) or MERIS and Sentinel-3/OLCI (300 m), the typical $R_{rs}(\lambda)$ of red tides provided in the present study could however advantageously complement previous approaches related to optical water type clustering (Moore et al., 2014; Vantrepotte et al., 2012; Wei et al., 2022) or satellite-based estimation of phytoplankton functional types (Mouw et al., 2017; Bracher et al., 2017), by providing examples of extreme endmembers. Alternatively, it could also be used to evaluate the performance of $R_{rs}(\lambda)$ classification methods (Ghatkar et al., 2019) in the case of massive red tides.

Due to the collation of red tides from the same phytoplankton genus in several geographic locations over several seasons and years, the bio-optical variability associated with eco-physiological driven processes were minored (i.e., interspecific optical variability as well as physiological changes or bio-regional biases). Several bloom-forming species were however absent from the red tide database. In particular, blooms dominated by diatoms, which were not included in the database because of the lack of massive events meeting the selection criteria, are likely to be part of the last optical bloom type (Fig. 9a) due to the presence of fucoxanthin. We recommend to continue the effort of compiling and updating the S2 red tide database, as more blooms will be documented in the next years. Furthermore, in order to improve the characterization of red tides $R_{rs}(\lambda)$, we also recommend to investigate the ability of high spatial resolution hyperspectral satellite missions (such as the recently launched Italian "*PRecursore IperSpettrale della Missione Applicativa*" (PRISMA) and German Environmental Mapping and Analysis Program (EnMAP) missions, as well as the future ESA Copernicus Hyperspectral Imaging Mission for the Environment (CHIME) and NASA Surface Biology and Geology (SBG) missions) to detect massive phytoplankton blooms.

Table 2
Standardized remote-sensing reflectance, as computed in Eq. (1), of the optical bloom types (OBT) shown in Fig. 3. OBT1 corresponds to a red tide dominated by *Prorocentrum* sp., *Gymnodinium* sp., *Lingulodinium polyedra*, *Gonyaulax* sp., *Alexandrium* sp., or *Anabaenopsis* sp. OBT2 corresponds to a red tide dominated by *Tripos fusus*, *Protoceratium reticulatum*, *Karlodinium veneficum*, *Aureococcus anophagefferens*, *Karenia* sp., *Phaeocystis* sp., or *Margalefidinium polykrikoides.* OBT3 corresponds to a red tide dominated by *Mesodinium rubrum*. OBT4 corresponds to a red tide dominated by *Lepidodinium chlorophorum*. OBT5 corresponds to a red tide dominated by the green *Noctiluca scintillans*, *Microcystis* sp., *Trichodesmium* sp., *Nodularia spumigena*, or *Aphanizomenon* sp. OBT6 corresponds to a red tide dominated by the red *Noctiluca scintillans*.

Wavelength (nm)	OBT1	OBT2	OBT3	OBT4	OBT5	OBT6
560	0.63178334	1.10130824	0.05561066	1.77247436	0.29041012	0.64270819
665	0.26812967	0.31244731	0.05801343	−0.07194668	0.04885253	0.70332681
704	2.50408597	2.33034944	2.43749154	1.76413907	0.76256485	0.73688903
740	1.07955521	0.56002202	0.66936968	0.00456138	1.41839545	0.73913184
783	1.00958199	0.55372242	0.52351892	−0.03880845	1.48733335	0.75834278
834	0.75747458	0.34137296	0.27509317	−0.14019092	1.41161258	0.78936494
865	0.40202742	0.14694422	−0.08650186	−0.32356164	1.36578262	0.65646161

4.2.2. Optical properties of massive phytoplankton blooms

Complementary to the approach developed in the present study, another way to develop an improved understanding of the reflectance fingerprint of harmful algal blooms is to characterize the inherent optical properties (IOPs) of monospecific phytoplankton culture, and to estimate the corresponding $R_{rs}(\lambda)$ using radiative transfer (Craig et al., 2006; Xi et al., 2015; Kim et al., 2016; Martinez-Vicente et al., 2020). The measurement of the scattering coefficient and phase function at the relevant spectral and angular resolutions is however extremely challenging (Harmel et al., 2016), and its incomplete characterization can yield significant biases in reflectance simulation (Xi et al., 2017; Harmel et al., 2021). With that respect, the $R_{rs}(\lambda)$ database of nearly monospecific massive blooms compiled in the present study could be useful to evaluate the results of radiative transfer modeling obtained by combining the IOPs of several types of microbial particles (e.g., Mobley and Stramski, 1997; Stramski and Mobley, 1997).

In previous studies, the detection of a given bloom-forming phytoplankton species was generally more efficient when using a classification metric computed from the absorption coefficient rather than from the remote-sensing reflectance (Craig et al., 2006; Xi et al., 2015). The interest of analysing the spectral differences between various phytoplankton assemblages using the absorption coefficient rather than $R_{rs}(\lambda)$ was also demonstrated in other studies (Torrecilla et al., 2011; Uitz et al., 2015). Interestingly, the present study provides an exception to such a rule. While the absorption coefficients of the phycoerythrin-bearing *M. rubrum* and *Trichodesmium* are quite similar (Dupouy et al., 2008; Guzmán et al., 2016), these two species were part of two different bloom optical types. For such a particular case, the $R_{rs}(\lambda)$-based clustering proved more useful to separate the two types of red tides due to significant differences in their vertical distribution (i.e. *Trichodesmium* can form surface scums on top of the water surface, whereas *M. rubrum* typically concentrate within a dense thin layer near the water surface) and/or scattering coefficient (Dupouy et al., 2008; McKinna, 2015; Guzmán et al., 2016).

The analysis of S2 red tide observations also made it possible to characterize $R_{rs}(\lambda)$ variations in the SWIR, a spectral range rarely characterized otherwise. Interestingly, dense surface accumulations of buoyant cyanobacteria such as *Trichodesmium* or *Microcystis* (Qi et al., 2020), as well as foam slicks associated with *Phaeocystis* blooms (Neukermans et al., 2018) displayed non-zero R_{rs}(1610 nm). While the existence of such high SWIR signal poses challenges to glint and atmospheric correction, it is also promising for the detection of massive HABs. The systematic inclusion of at least one SWIR band is therefore strongly recommended for the next generation of both multi- and hyperspectral satellite sensors.

5. Conclusion

More than 100 red tides were documented worldwide using an original combination of in situ monitoring data together with S2 high spatial resolution remote sensing. The S2 red tide database covered 27 phytoplankton bloom-forming species, and was dominated by dinoflagellates and cyanobacteria. A hierarchical cluster analysis determined 6 optical bloom types with distinct reflectance shapes. Due to their unique pigment composition, red tides of *M. rubrum* (a phycoerythrin-bearing mixotrophic ciliate), green seawater discolorations of *L. chlorophorum* (a dinoflagellate with an unusual carotenoid composition), and red-orange surface aggregation of the red *N. scintillans* (a purely heterotrophic dinoflagellate devoid of Chl *a*) constituted 3 monospecific bloom clusters with unique reflectance fingerprint. Surface accumulations of buoyant cyanobacteria dominated another bloom optical type with a red-edge feature typical of floating algae (high NIR $R_{rs}(\lambda)$ plateau, with several species also characterized by non-zero SWIR $R_{rs}(\lambda)$). Surface aggregations of the green *N. scintillans*, which contain Chl *a* due to a photosynthetic symbiont, were also part of this cluster. The last two clusters were taxonomically and spectrally more diverse. One cluster was dominated by blooms of dinoflagellates such as *Lingulodinium polyedra*, whereas the other cluster contained blooms caused by a dinoflagellate such as *Karenia brevis*, as well as by a prymnesiophyte (*Phaeocystis*) or a pelagophyte (*A. anophagefferens*).

By providing a comprehensive assessment of the reflectance variability underlying the many shades of red tides worldwide, the present study clearly demonstrated S2 ability to study highly concentrated phytoplankton blooms. It offers original perspectives for future studies, such as the potentiality to remotely recognize the dominant optical bloom type in the absence of in situ taxonomic data. This study has practical implications for HAB detection, and it is expected that our results will prompt monitoring agencies to systematically complement field sampling with the analysis of S2 observations, when possible. Eventually, as a similar "library-building" approach could be applied to other sensors (provided that their spatial resolution is high enough to consistently capture the small-scale features of highly concentrated phytoplankton patches in coastal waters), it is expected that the advent of high-resolution hyperspectral satellite missions such as PRISMA, EnMAP, SBG or CHIME will allow an enhanced detection of red tides diversity in the near future. There is no doubt that such instrumental progress will pave the way toward an increased understanding of the ecological processes underlying massive blooms, thus being beneficial to both plankton ecologists and water quality managers.

Funding

This work was funded by the Centre National d' Etudes Spatiales (CNES, France) during the TOSCA project *LAboratory to Satellite experiments for remote sensing of Harmful Algae* (LASHA). This research was also supported by the grants RTI2018-098784-J-I00 and IJC2019-039382-I from the MCIN/AEI/10.13039/501100011033, by the European Regional Development Fund (ERDF) "A way of making Europe", as well as by the Andalusian Regional Government (project PY20-00244).

Author contributions

PG: conceptualization, database compilation, statistical analyses, writing - original draft, funding acquisition, project administration. MLZ: conceptualization, database compilation, processing of satellite data, writing - review & editing. TH: conceptualization, database compilation, processing of satellite data, writing - review & editing. TL: conceptualization, writing - review & editing. THF, GN, IC: database compilation, writing - review & editing.

Declaration of Competing Interest

The authors declare that they have no known competing financial interests or personal relationships that could have appeared to influence the work reported in this paper.

Data availability

Data will be made available on request.

Acknowledgements

The authors thank all contributors to the HAEDAT and REPHY databases: this work would have never been possible without the long-term dedicated efforts of so many plankton experts worldwide. In particular, PG expresses his sincere thanks to Michaël Retho and Olivier Pierre-Duplessix, as well as to the whole team from IFREMER LER/MPL for tirelessly sampling phytoplankton blooms off the Loire and Vilaine estuaries. Amelia Curd and Anne Doner (IFREMER), coordinators of the Phenomer citizen project, are acknowledged for sharing information about seawater discolorations in Brittany. Raphaël Grisel, Nicolas Mayot, and Beatriz Beker are thanked for sharing phytoplankton data

from the Berre lagoon. The author of the blog Fitopasión is thanked for the provision of very informative posts. The team "Eyes over Puget Sound" of the department of Ecology from the state of Washington is acknowledged for making available regular airborne surveys and in situ reports of seawater discolorations. Jennifer Wolny (Maryland Department of Natural Resources), as well as Michelle Tomlinson and Rick Stumpf (NOAA) are thanked for interesting discussions about red tides in Chesapeake Bay. PG is grateful to Kenneth Mertens (IFREMER LER/BO) and all participants of the Dino12 conference for stimulating scientific exchanges about dinoflagellates ecology and taxonomy. We are grateful to Victor Pochic for preparing the culture of the cryptophyte *Teleaulax amphioxeia*, and providing phycoerythrin extract. Finally, four anonymous reviewers are acknowledged for their detailed comments, which significantly improved the manuscript.

Appendix A. Supplementary data

The supplementary information contains three types of material: (1) a text document with the evaluation of atmospheric correction performance, (2) a table with the detailed list of the 108 blooms including the date, location, reference, and taxonomic details, and (3) a list of figures showing the reflectance spectra, as well as examples of RGB and REGB images, of the 108 bloom events. Supplementary data to this article can be found online at https://doi.org/10.1016/j.rse.2023.113486.

References

Anderson, D.M., 2009. Approaches to monitoring, control and management of harmful algal blooms (HABs). Ocean Coast. Manage. 52, 342–347.
Anderson, C.R., Berdalet, E., Kudela, R.M., Cusack, C.K., Silke, J., O'Rourke, E., Morell, J., 2019. Scaling up from regional case studies to a global harmful algal bloom observing system. Front. Mar. Sci. 250.
Astoreca, R., Rousseau, V., Ruddick, K., Van Mol, B., Parent, J.Y., Lancelot, C., 2005. Optical properties of algal blooms in an eutrophicated coastal area and its relevance to remote sensing. Remote Sens. Coastal Ocean. Environ. 5885, 245–255.
Balch, W.M., Haxo, F.T., 1984. Spectral properties of Noctiluca miliaris suriray, a heterotrophic dinoflagellate. J. Plankton Res. 6, 515–525.
Belin, C., Soudant, D., Amzil, Z., 2021. Three decades of data on phytoplankton and phycotoxins on the french coast: lessons from REPHY and REPHYTOX. Harmful Algae 102, 101733.
Berdalet, E., Fleming, L.E., Gowen, R., Davidson, K., Hess, P., Backer, L.C., Enevoldsen, H., 2016. Marine harmful algal blooms, human health and wellbeing: challenges and opportunities in the 21st century. J. Mar. Biol. Assoc. UK 96, 61–91.
Bergman, B., Sandh, G., Lin, S., Larsson, J., Carpenter, E.J., 2013. Trichodesmium–a widespread marine cyanobacterium with unusual nitrogen fixation properties. FEMS Microbiol. Rev. 37, 286–302.
Bracher, A., Bouman, H.A., Brewin, R.J., Bricaud, A., Brotas, V., Ciotti, A.M., Wolanin, A., 2017. Obtaining phytoplankton diversity from ocean color: a scientific roadmap for future development. Front. Mar. Sci. 4, 55.
Bramich, J., Bolch, C.J., Fischer, A., 2021. Improved red-edge chlorophyll-a detection for sentinel 2. Ecol. Ind. 120, 106876.
Blondeau-Patissier, D., Gower, J.F.R., Dekker, A.G., Phinn, S.R., Brando, V.E., 2014. A review of ocean color remote sensing methods and statistical techniques for the detection, mapping and analysis of phytoplankton blooms in coastal and open oceans. Prog. Oceanogr. 123, 123–144.
Blondeau-Patissier, D., Brando, V.E., Lønborg, C., Leahy, S.M., Dekker, A.G., 2018. Phenology of trichodesmium spp. Blooms in the great barrier reef lagoon, Australia, from the ESA-MERIS 10-year mission. PloS One 13, e0208010.
Bricaud, A., Claustre, H., Ras, J., Oubelkheir, K., 2004. Natural variability of phytoplanktonic absorption in oceanic waters: influence of the size structure of algal populations. J. Geophys. Res. Oceans 109 (C11).
Brown, A.R., Lilley, M., Shutler, J., Lowe, C., Artioli, Y., Torres, R., Tyler, C.R., 2020. Assessing risks and mitigating impacts of harmful algal blooms on mariculture and marine fisheries. Rev. Aquacult. 12, 1663–1688.
Bulit, C., Díaz-Ávalos, C., Montagnes, D.J., 2004. Assessing spatial and temporal patchiness of the autotrophic ciliate *Myrionecta rubra*: a case study in a coastal lagoon. Mar. Ecol. Prog. Ser. 268, 55–67.
Caballero, I., Fernández, R., Escalante, O.M., Mamán, L., Navarro, G., 2020. New capabilities of sentinel-2A/B satellites combined with in situ data for monitoring small harmful algal blooms in complex coastal waters. Sci. Rep. 10, 1–14.
Caballero, I., Navarro, G., 2021. Monitoring cyanoHABs and water quality in Laguna Lake (Philippines) with Sentinel-2 satellites during the 2020 Pacific typhoon season. Sci. Tot. Environ. 788, 147700.
Caballero, I., Roca, M., Santos-Echeandía, J., Bernárdez, P., Navarro, G., 2022. Use of the Sentinel-2 and Landsat-8 satellites for water quality monitoring: an early warning tool in the mar menor coastal lagoon. Remote Sens. 14, 2744.
Capone, D.G., 2021. Coming full circle on diazotrophy in the marine cyanobacterium trichodesmium. Proc. Nat. Academy Sci. 118, e2117967118.
Carder, K.L., Steward, R.G., 1985. A remote-sensing reflectance model of a red-tide dinoflagellate off West Florida. Limnol. Oceanogr. 30, 286–298.
Clementson, L.A., Wojtasiewicz, B., 2019. Dataset on the absorption characteristics of extracted phytoplankton pigments. Data Brief 24, 103875.
Cloern, J.E., Jassby, A.D., 2010. Patterns and scales of phytoplankton variability in estuarine–coastal ecosystems. Estuar. Coasts 33, 230–241.
Conejo-Orosa, T., Caballero-Herrera, J.A., Castro-Claros, J.D., Pino-de la Torre, L., Pozzo-Pirotta, L.J., Sellés-Rıos, B., Garcıa-Gómez, C.A., 2019. Mesodinium rubrum (ciliate) red tide in the Alboran Sea. II Congreso Jóvenes Investigadors del Mar, 1 - 4 Oct. 2019, Malaga (Spain).
Craig, S.E., Lohrenz, S.E., Lee, Z., Mahoney, K.L., Kirkpatrick, G.J., Schofield, O.M., Steward, R.G., 2006. Use of hyperspectral remote sensing reflectance for detection and assessment of the harmful alga, karenia brevis. Appl. Opt. 45, 5414–5425.
Crawford, D.W., 1989. Mesodinium rubrum: the phytoplankter that wasn't. Mar. Ecol. Prog. Ser. 58, 161–174.
Darwin, C., 1839. Narrative of the surveying voyages of His Majesty's ships adventure and Beagle, between the years 1826-36, describing their examination of the southern shores of South America, and the Beagle circumnavigation of the globe. In: Journal and Remarks, Vol. III. Henry Colburn, London.
Díaz, P.A., Peréz-Santos, I., Álvarez, G., Garreaud, R., Pinilla, E., Díaz, M., Reguera, B., 2021. Multiscale physical background to an exceptional harmful algal bloom of Dinophysis acuta in a fjord system. Sci. Tot. Environ. 773, 145621.
Dierssen, H.M., Kudela, R.M., Ryan, J.P., Zimmerman, R.C., 2006. Red and black tides: quantitative analysis of water-leaving radiance and perceived color for phytoplankton, colored dissolved organic matter, and suspended sediments. Limnol. Oceanogr. 51, 2646–2659.
Dolatabadi, F., Attaran-Fariman, G., Loghmani, M., 2021. Bloom occurrence and phylogeny of Gonyaulax polygramma (Dinophyceae) isolated from south east coast of Iran (Oman Sea). Iran. J. Fisheries Sci. 20, 1789–1803.
Dupouy, C., Neveux, J., Dirberg, G., Rottgers, R., Tenório, M.B., Ouillon, S., 2008. Bio-optical properties of the marine cyanobacteria trichodesmium spp. J. Appl. Remote. Sens. 2, 023503.
Ericson, K., 2017. Making space for red tide: discolored water and the early twentieth century bayscape of japanese pearl cultivation. J. Hist. Biol. 50, 393–423.
Elbrächter, M., Schnepf, E., 1996. Gymnodinium chlorophorum, a new, green, bloom-forming dinoflagellate (Gymnodiniales, Dinophyceae) with a vestigial prasinophyte endosymbiont. Phycologia 35, 381–393.
Elbrächter, M., Qi, Z., 1998. Aspects of noctiluca (Dinophyceae) population dynamics. In: Anderson, D.M., Cembella, A.D., Hallegraeff, G.M. (Eds.), Physiological Ecology of Harmful Algal Blooms. Springer, Berlin, pp. 315–335.
Ershadifar, H., Koochaknejad, E., Ghazilou, A., Kor, K., Negarestan, H., Baskaleh, G., 2020. Response of phytoplankton assemblages to variations in environmental parameters in a subtropical bay (Chabahar Bay, Iran): harmful algal blooms and coastal hypoxia. Reg. Stud. Mar. Sci. 39, 101421.
Fenchel, T., 1968. On "red water" in the isefjord (inner danish waters) caused by the ciliate Mesodinium rubrum. Ophelia 5, 245–253.
Franks, P.J., 1992. Phytoplankton blooms at fronts: patterns, scales, and physical forcing mechanisms. Rev. Aquat. Sci. 6, 121–137.
Ghatkar, J.G., Singh, R.K., Shanmugam, P., 2019. Classification of algal bloom species from remote sensing data using an extreme gradient boosted decision tree model. Int. J. Remote Sens. 40, 9412–9438.
Gitelson, A., 1992. The peak near 700 nm on radiance spectra of algae and water: relationships of its magnitude and position with chlorophyll concentration. Int. J. Remote Sens. 13, 3367–3373.
Glibert, P.M., 2017. Eutrophication, harmful algae and biodiversity - challenging paradigms in a world of complex nutrient changes. Mar. Pollut. Bull. 124, 591–606.
Gower, J.F.R., Denman, K.L., Holyer, R.J., 1980. Phytoplankton patchiness indicates the fluctuation spectrum of mesoscale oceanic structure. Nature 288, 157–159.
Gower, J., King, S., Goncalves, P., 2008. Global monitoring of plankton blooms using MERIS MCI. Int. J. Remote Sens. 29, 6209–6216.
Goy, J., 2003. La mer dans l'Odyssée. Gaia 7, 225–231.
Gustafson, D.E., Stoecker, D.K., Johnson, M.D., Van Heukelem, W.F., Sneider, K., 2000. Cryptophyte algae are robbed of their organelles by the marine ciliate Mesodinium rubrum. Nature 405, 1049–1052.
Guzmán, L., Varela, R., Muller-Karger, F., Lorenzoni, L., 2016. Bio-optical characteristics of a red tide induced by Mesodinium rubrum in the Cariaco Basin, Venezuela. J. Mar. Syst. 160, 17–25.
Hallegraeff, G.M., 1993. A review of harmful algal blooms and their apparent global increase. Phycologia 32, 79–99.
Hallegraeff, G.M., 2003. Harmful algal blooms: a global overview. In: Manual on Harmful Marine Microalgae, 33, pp. 1–22.
Hallegraeff, G.M., Anderson, D.M., Belin, C., Bottein, M.Y.D., Bresnan, E., Chinain, M., Zingone, A., 2021. Perceived global increase in algal blooms is attributable to intensified monitoring and emerging bloom impacts. Comm. Earth Environ. 2, 1–10.
Harke, M.J., Steffen, M.M., Gobler, C.J., Otten, T.G., Wilhelm, S.W., Wood, S.A., Paerl, H. W., 2016. A review of the global ecology, genomics, and biogeography of the toxic cyanobacterium, microcystis spp. Harmful Algae 54, 4–20.
Harmel, T., Hieronymi, M., Slade, W., Röttgers, R., Roullier, F., Chami, M., 2016. Laboratory experiments for inter-comparison of three volume scattering meters to measure angular scattering properties of hydrosols. Opt. Express 24, A234–A256.
Harmel, T., Chami, M., Tormos, T., Reynaud, N., Danis, P.A., 2018. Sunglint correction of the multi-spectral instrument (MSI)-Sentinel-2 imagery over inland and sea waters from SWIR bands. Remote Sens. Environ. 204, 308–321.
Harmel, T., Agagliate, J., Hieronymi, M., Gernez, P., 2021. Two-term Reynolds–McCormick phase function parameterization better describes light scattering by microalgae and mineral hydrosols. Opt. Lett. 46, 1860–1863.

Harred, L.B., Campbell, L., 2014. Predicting harmful algal blooms: a case study with Dinophysis ovum in the Gulf of Mexico. J. Plankton Res. 36, 1434–1445.
Harrison, P.J., Furuya, K., Glibert, P.M., Xu, J., Liu, H.B., Yin, K., Ho, A.Y.T., 2011. Geographical distribution of red and green Noctiluca scintillans. Chin. J. Oceanol. Lim. 29, 807–831.
Hart, T., 1934. Red water-bloom in south african seas. Nature 134, 459–460.
Hart, T., 1943. Darwin and "water-bloom". Nature 152, 661–662.
Herfort, L., Peterson, T.D., Campbell, V., Futrell, S., Zuber, P., 2011. Myrionecta rubra (Mesodinium rubrum) bloom initiation in the Columbia River estuary. Estuar. Coast. Shelf Sci. 95, 440–446.
IOCCG, 2021. Observation of harmful algal blooms with ocean colour radiometry. In: Bernard, S., Kudela, R., Robertson Lain, L., Pitcher, G.C. (Eds.), IOCCG Report Series, No. 20. International Ocean Colour Coordinating Group, Dartmouth, Canada.
Johnson, M.D., Stoecker, D.K., Marshall, H.G., 2013. Seasonal dynamics of Mesodinium rubrum in Chesapeake Bay. J. Plankton Res. 35, 877–893.
Kahru, M., Savchuk, O.P., Elmgren, R., 2007. Satellite measurements of cyanobacterial bloom frequency in the Baltic Sea: interannual and spatial variability. Mar. Ecol. Prog. Ser. 343, 15–23.
Kahru, M., Anderson, C., Barton, A.D., Carter, M.L., Catlett, D., Send, U., Mitchell, B.G., 2021. Satellite detection of dinoflagellate blooms off California by UV reflectance ratios. Elem. Sci. Anth. 9, 00157.
Karlson, B., Andersen, P., Arneborg, L., Cembella, A., Eikrem, W., John, U., Suikkanen, S., 2021. Harmful algal blooms and their effects in coastal seas of northern Europe. Harmful Algae 102, 101989.
Kim, Y., Yoo, S., Son, Y.B., 2016. Optical discrimination of harmful Cochlodinium polykrikoides blooms in korean coastal waters. Opt. Express 24, A1471–A1488.
Kutser, T., 2004. Quantitative detection of chlorophyll in cyanobacterial blooms by satellite remote sensing. Limnol. Oceanogr. 49, 2179–2189.
Kutser, T., Metsamaa, L., Strömbeck, N., Vahtmäe, E., 2006. Monitoring cyanobacterial blooms by satellite remote sensing. Estuarine Coast. Shelf Sci. 67, 303–312.
Landsberg, J.H., Flewelling, L.J., Naar, J., 2009. Karenia brevis red tides, brevetoxins in the food web, and impacts on natural resources: decadal advancements. Harmful Algae 8, 598–607.
Lassus, P., Chomérat, N., Hess, P., Nézan, E., 2016. Toxic and harmful microalgae of the world ocean. In: International Society for the Study of Harmful Algae / Intergovernmental Oceanographic Commission of UNESCO. IOC Manuals and Guides, p. 68.
Mafra Jr., L.L., Nolli, P.K.W., Mota, L.E., Domit, C., Soeth, M., Luz, L.F.G., Di Domenico, M., 2019. Multi-species okadaic acid contamination and human poisoning during a massive bloom of Dinophysis acuminata complex in southern Brazil. Harmful Algae 89, 101662.
Martinez-Vicente, V., Kurekin, A., Sá, C., Brotas, V., Amorim, A., Veloso, V., Miller, P.I., 2020. Sensitivity of a satellite algorithm for harmful algal bloom discrimination to the use of laboratory bio-optical data for training. Front. Mar. Sci. 7, 582960.
Matthews, M.W., Bernard, S., Robertson, L., 2012. An algorithm for detecting trophic status (chlorophyll-a), cyanobacterial-dominance, surface scums and floating vegetation in inland and coastal waters. Remote Sens. Environ. 124, 637–652.
McKinna, L.I., Furnas, M.J., Ridd, P.V., 2011. A simple, binary classification algorithm for the detection of trichodesmium spp. Within the great barrier reef using MODIS imagery. Limnol. Oceanogr. Meth. 9, 50–66.
McKinna, L.I., 2015. Three decades of ocean-color remote-sensing trichodesmium spp. In the World's oceans: a review. Prog. Oceanogr. 131, 177–199.
Millie, D.F., Schofield, O.M., Kirkpatrick, G.J., Johnsen, G., Tester, P.A., Vinyard, B.T., 1997. Detection of harmful algal blooms using photopigments and absorption signatures: a case study of the Florida red tide dinoflagellate, Gymnodinium breve. Limnol. Oceanogr. 42, 1240–1251.
Mishra, S., Mishra, D.R., 2012. Normalized difference chlorophyll index: a novel model for remote estimation of chlorophyll-a concentration in turbid productive waters. Remote Sens. Environ. 117, 394–406.
Mobley, C.D., Stramski, D., 1997. Effects of microbial particles on oceanic optics: methodology for radiative transfer modeling and example simulations. Limnol. Oceanogr. 42, 550–560.
Montagnes, D.J., Poulton, A.J., Shammon, T.M., 1999. Mesoscale, finescale and microscale distribution of micro-and nanoplankton in the Irish Sea, with emphasis on ciliates and their prey. Mar. Biol. 134, 167–179.
Moore, T.S., Dowell, M.D., Bradt, S., Verdu, A.R., 2014. An optical water type framework for selecting and blending retrievals from bio-optical algorithms in lakes and coastal waters. Remote Sens. Environ. 143, 97–111.
Moore, T.S., Mouw, C.B., Sullivan, J.M., Twardowski, M.S., Burtner, A.M., Ciochetto, A. B., Weidemann, A., 2017. Bio-optical properties of cyanobacteria blooms in western Lake Erie. Front. Mar. Sci. 4, 300.
Mouw, C.B., Hardman-Mountford, N.J., Alvain, S., Bracher, A., Brewin, R.J., Bricaud, A., Uitz, J., 2017. A consumer's guide to satellite remote sensing of multiple phytoplankton groups in the global ocean. Front. Mar. Sci. 4, 41.
Muller-Karger, F.E., Hestir, E., Ade, C., Turpie, K., Roberts, D.A., Siegel, D., Jetz, W., 2018. Satellite sensor requirements for monitoring essential biodiversity variables of coastal ecosystems. Ecol. Appl. 28, 749–760.
Neukermans, G., Harmel, T., Galí, M., Rudorff, N., Chowdhary, J., Dubovik, O., Miller, L. A., 2018. Harnessing remote sensing to address critical science questions on ocean-atmosphere interactions. Elem. Sci. Anth. 6, 71.
Pahlevan, N., Mangin, A., Balasubramanian, S.V., Smith, B., Alikas, K., Arai, K., Warren, M., 2021. ACIX-aqua: a global assessment of atmospheric correction methods for Landsat-8 and Sentinel-2 over lakes, rivers, and coastal waters. Remote Sens. Environ. 258, 112366.
Park, M.G., Kim, S., Kim, H.S., Myung, G., Kang, Y.G., Yih, W., 2006. First successful culture of the marine dinoflagellate Dinophysis acuminata. Aquat. Microb. Ecol. 45, 101–106.
Pitcher, G.C., Foord, C.J., Macey, B.M., Mansfield, L., Mouton, A., Smith, M.E., van der Molen, L., 2019. Devastating farmed abalone mortalities attributed to yessotoxin-producing dinoflagellates. Harmful Algae 81, 30–41.
Qi, L., Tsai, S.F., Chen, Y., Le, C., Hu, C., 2019. In search of red Noctiluca scintillans blooms in the East China Sea. Geophys. Res. Lett. 46, 5997–6004.
Qi, L., Hu, C., Mikelsons, K., Wang, M., Lance, V., Sun, S., Van der Zande, D., 2020. In search of floating algae and other organisms in global oceans and lakes. Remote Sens. Environ. 239, 111659.
Quibell, G., 1992. Estimating chlorophyll concentrations using upwelling radiance from different freshwater algal genera. Int. J. Remote Sens. 13, 2611–2621.
Reguera, B., Velo-Suárez, L., Raine, R., Park, M.G., 2012. Harmful dinophysis species: a review. Harmful Algae 14, 87–106.
Rial, P., Garrido, J.L., Jaén, D., Rodríguez, F., 2013. Pigment composition in three dinophysis species (Dinophyceae) and the associated cultures of Mesodinium rubrum and teleaulax amphioxeia. J. Plankton Res. 35, 433–437.
Rodríguez-Benito, C.V., Navarro, G., Caballero, I., 2020. Using copernicus Sentinel-2 and Sentinel-3 data to monitor harmful algal blooms in southern Chile during the COVID-19 lockdown. Mar. Pollut. Bull. 161, 111722.
Roux, P., Siano, R., Collin, K., Bilien, G., Sinquin, C., Marchand, L., Schapira, M., 2021. Bacteria enhance the production of extracellular polymeric substances by the green dinoflagellate lepidodinium chlorophorum. Sci. Rep. 11, 1–15.
Roux, P., Siano, R., Souchu, P., Collin, K., Schmitt, A., Manach, S., Schapira, M., 2022. Spatio-temporal dynamics and biogeochemical properties of green seawater discolorations caused by the marine dinoflagellate Lepidodinium chlorophorum along southern Brittany coast. Estuar. Coast. Shelf Sci. 107950.
Ryther, J.H., 1955. Ecology of autotrophic marine dinoflagellates with reference to red water conditions. In: Johnson, F.H. (Ed.), The Luminescence of Biological Systems; Proceedings of the Conference on Luminescence. American Association for the Advancement of Science, Washington (US), pp. 347–413.
Ryther, J.H., 1967. Occurrence of red water off Peru. Nature 214, 1318–1319.
Smith, M.E., Bernard, S., 2020. Satellite ocean color based harmful algal bloom indicators for aquaculture decision support in the southern Benguela. Front. Mar. Sci. 61.
Siano, R., Chapelle, A., Antoine, V., Michel-Guillou, E., Rigaut-Jalabert, F., Guillou, L., Curd, A., 2020. Citizen participation in monitoring phytoplankton seawater discolorations. Mar. Pol. 117, 103039.
Smayda, T.J., 1997a. Harmful algal blooms: their ecophysiology and general relevance to phytoplankton blooms in the sea. Limnol. Oceanogr. 42, 1137–1153.
Smayda, T.J., 1997b. What is a bloom? A commentary. Limnol. Oceanogr. 42, 1132–1136.
Soja-Woźniak, M., Darecki, M., Wojtasiewicz, B., Bradtke, K., 2018. Laboratory measurements of remote sensing reflectance of selected phytoplankton species from the Baltic Sea. Oceanologia 60, 86–96.
Souchu, P., Retho, M., Schapira, M., Fortune, M., Manach, S., Schmitt, A., Cochennec-Laureau, N., 2017. Note sur les eaux colorées observées au large de la Loire et de la Vilaine en avril 2017.
Sourisseau, M., Jegou, K., Lunven, M., Quere, J., Gohin, F., Bryere, P., 2016. Distribution and dynamics of two species of dinophyceae producing high biomass blooms over the french Atlantic shelf. Harmful Algae 53, 53–63.
Sournia, A., Belin, C., Billard, C., Catherine, M., Denn, E.L., Fresnel, J., Soulard, R., 1992. The repetitive and expanding occurrence of a green, bloom-forming dinoflagellate (Dinophyceae) on the coasts of France. Cryptogamie Algol. 13, 1–13.
Sournia, A., 1995. Red tide and toxic marine phytoplankton of the world ocean: an inquiry into biodiversity. In: Harmful Marine Algal Blooms, Proc. 6th Int. Conf. on Toxic Marine Phytoplankton. Lavoisier., pp. 103–112.
Spyrakos, E., Odonnell, R., Hunter, P.D., Miller, C., Scott, M., Simis, S.G., Tyler, A.N., 2018. Optical types of inland and coastal waters. Limnol. Oceanogr. 63, 846–870.
Stramski, D., Mobley, C.D., 1997. Effects of microbial particles on oceanic optics: a database of single-particle optical properties. Limnol. Oceanogr. 42, 538–549.
Schaeffer, B.A., Myer, M.H., 2020. Resolvable estuaries for satellite derived water quality within the continental United States. Remote Sens. Lett. 11, 535–544.
Stumpf, R.P., Culver, M.E., Tester, P.A., Tomlinson, M., Kirkpatrick, G.J., Pederson, B.A., Soracco, M., 2003. Monitoring karenia brevis blooms in the Gulf of Mexico using satellite ocean color imagery and other data. Harmful Algae 2, 147–160.
Tomlinson, M.C., Wynne, T.T., Stumpf, R.P., 2009. An evaluation of remote sensing techniques for enhanced detection of the toxic dinoflagellate, Karenia brevis. Remote Sens. Environ. 113, 598–609.
Torrecilla, E., Stramski, D., Reynolds, R.A., Millán-Núñez, E., Piera, J., 2011. Cluster analysis of hyperspectral optical data for discriminating phytoplankton pigment assemblages in the open ocean. Remote Sens. Environ. 115, 2578–2593.
Uitz, J., Stramski, D., Reynolds, R.A., Dubranna, J., 2015. Assessing phytoplankton community composition from hyperspectral measurements of phytoplankton absorption coefficient and remote-sensing reflectance in open-ocean environments. Remote Sens. Environ. 171, 58–74.
Vantrepotte, V., Loisel, H., Dessailly, D., Mériaux, X., 2012. Optical classification of contrasted coastal waters. Remote Sens. Environ. 123, 306–323.
Wells, M.L., Trainer, V.L., Smayda, T.J., Karlson, B.S., Trick, C.G., Kudela, R.M., Cochlan, W.P., 2015. Harmful algal blooms and climate change: learning from the past and present to forecast the future. Harmful Algae 49, 68–93.
Wei, J., Wang, M., Mikelsons, K., Jiang, L., Kratzer, S., Lee, Z., Van der Zande, D., 2022. Global satellite water classification data products over oceanic, coastal, and inland waters. Remote Sens. Environ. 282, 113233.

Wells, M.L., Karlson, B., Wulff, A., Kudela, R., Trick, C., Asnaghi, V., Trainer, V.L., 2020. Future HAB science: directions and challenges in a changing climate. Harmful Algae 91, 101632.
Wolny, J.L., Tomlinson, M.C., Schollaert Uz, S., Egerton, T.A., McKay, J.R., Meredith, A., Stumpf, R.P., 2020. Current and future remote sensing of harmful algal blooms in the Chesapeake Bay to support the shellfish industry. Front. Mar. Sci. 7, 337.
Xi, H., Hieronymi, M., Röttgers, R., Krasemann, H., Qiu, Z., 2015. Hyperspectral differentiation of phytoplankton taxonomic groups: a comparison between using remote sensing reflectance and absorption spectra. Remote Sens. 7, 14781–14805.
Xi, H., Hieronymi, M., Krasemann, H., Röttgers, R., 2017. Phytoplankton group identification using simulated and in situ hyperspectral remote sensing reflectance. Front. Mar. Sci. 4, 272.
Yih, W., Kim, H.S., Jeong, H.J., Myung, G., Kim, Y.G., 2004. Ingestion of cryptophyte cells by the marine photosynthetic ciliate Mesodinium rubrum. Aquat. Microb. Ecol. 36, 165–170.
Yih, W., Kim, H.S., Myung, G., Park, J.W., Du Yoo, Y., Jeong, H.J., 2013. The red-tide ciliate Mesodinium rubrum in korean coastal waters. Harmful Algae 30, S53–S61.
Zapata, M., Fraga, S., Rodríguez, F., Garrido, J.L., 2012. Pigment-based chloroplast types in dinoflagellates. Mar. Ecol. Progr. Ser. 465, 33–52.